

DISSERTATION

ON THE ROLE OF WARM RAIN CLOUDS IN THE TROPICS

Submitted by

Anita Denise Rapp

Department of Atmospheric Science

In partial fulfillment of the requirements

For the degree of Doctor of Philosophy

Colorado State University

Fort Collins, Colorado

Fall 2008

UMI Number: 3346469

INFORMATION TO USERS

The quality of this reproduction is dependent upon the quality of the copy submitted. Broken or indistinct print, colored or poor quality illustrations and photographs, print bleed-through, substandard margins, and improper alignment can adversely affect reproduction.

In the unlikely event that the author did not send a complete manuscript and there are missing pages, these will be noted. Also, if unauthorized copyright material had to be removed, a note will indicate the deletion.

UMI[®]

UMI Microform 3346469

Copyright 2009 by ProQuest LLC.

All rights reserved. This microform edition is protected against unauthorized copying under Title 17, United States Code.

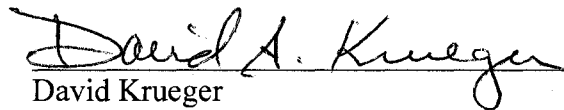
ProQuest LLC
789 E. Eisenhower Parkway
PO Box 1346
Ann Arbor, MI 48106-1346

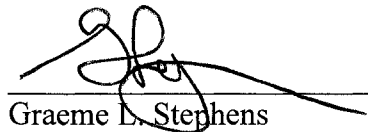
COLORADO STATE UNIVERSITY

October 28, 2008

WE HEREBY RECOMMEND THAT THE DISSERTATION PREPARED UNDER OUR SUPERVISION BY ANITA RAPP ENTITLED ON THE ROLE OF WARM RAIN CLOUDS IN THE TROPICS BE ACCEPTED AS FULLFILING IN PART REQUIREMENTS FOR THE DEGREE OF DOCTOR OF PHILOSOPHY.

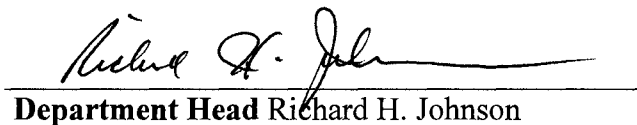
Committee on Graduate Work


David Krueger


Graeme L. Stephens


Thomas H. Vonder Haar


Advisor Christian D. Kummerow


Department Head Richard H. Johnson

ABSTRACT OF DISSERTATION

ON THE ROLE OF WARM RAIN CLOUDS IN THE TROPICS

A combined optimal estimation retrieval algorithm has been developed for warm rain clouds using Tropical Rainfall Measuring Mission (TRMM) satellite measurements. The algorithm uses TRMM Microwave Imager (TMI) brightness temperatures that have been deconvolved to the 19-GHz field-of-view (FOV) to retrieve cloud liquid water path (LWP), total precipitable water, and wind speed. Resampling the TMI measurements to a common FOV is found to decrease retrieved LWP by 30%.

These deconvolved brightness temperatures are combined with cloud fraction from the Visible Infrared Scanner (VIRS) to overcome the beam-filling effects and with rainwater estimates from the TRMM Precipitation Radar (PR). This algorithm is novel in that it takes into account the water in the rain and retrieves the LWP due to only the cloud water in a raining cloud, thus allowing the investigation of the effects of precipitation on cloud properties. The uncertainties due to forward model parameters and assumptions are computed and range from 1.7 K at 10 GHz to about 6K at the 37 and 85 GHz TMI channels. Examination of the sensitivities in the LWP retrieval shows that the cloud fraction information increases the retrieved LWP with decreasing cloud fraction and that the PR rainwater reduces retrieved LWP.

Retrieval algorithm results from December 2005 to January 2006 show that warm rain cloud LWP and the ratio of warm rain cloud LWP to rainwater both decrease by 50% over sea surface temperatures (SST) ranging from 292 to 302 K in the tropical western Pacific due to increased precipitation efficiency depleting more of the cloud water at higher SSTs.

The LWP retrieval developed in this study is also applied to study the influence of warm rain clouds on atmospheric preconditioning for deep convection associated with tropical depression-type disturbances (TDs). Results show that positive warm rain cloud LWP anomalies occur with positive low-level moistening and heating anomalies prior to TD events, but that there is little variation in the properties of non-raining clouds. The moistening by these clouds is also shown to influence the generation of convective available potential energy (CAPE) prior to deep convection.

Anita D. Rapp
Department of Atmospheric Science
Colorado State University
Fort Collins, CO 80523
Fall 2008

Acknowledgements

I would like to express my appreciation to my advisor, Professor Chris Kummerow, for his guidance and financial support for the last six years. I would also like to thank the Kummerow research group for their help and suggestions. I would like to convey my gratitude to my committee members, Professors David Krueger, Graeme Stephens, and Tom Vonder Haar, for their helpful comments and for taking the time to serve on my committee. Last, I would like to express to my family and my husband, Oliver Frauenfeld, how grateful I am that they continued to put up with me after I spent so many years as a student.

TABLE OF CONTENTS

<u>Chapter</u>		<u>Page</u>
1	Introduction	1
	1.1 Motivation	1
	1.2 Warm Rain Clouds	2
	1.3 Cloud Property Retrievals	3
	1.4 Current Study	6
2	On the Consequences of Resampling Microwave Radiometer Observations for Use in Retrieval Algorithms	9
	2.1 Introduction	9
	2.2 Deconvolution Method	11
	2.3 Retrieval and Results	15
	2.4 Synthetic Tests	20
	2.5 Retrieval without 85-GHz Channels	29
	2.6 Discussion	30
3	A Combined Multi-Sensor Optimal Estimation Retrieval Algorithm for Oceanic Warm Rain Clouds	33
	3.1 Introduction	33
	3.2 Data	40
	3.2.1 <i>Microwave Sensor</i>	40
	3.2.2 <i>Visible/Infrared Sensor</i>	41
	3.2.3 <i>Precipitation Radar</i>	42
	3.2.4 <i>Ancillary Data</i>	43
	3.3 Retrieval Algorithm	44
	3.3.1 <i>Forward Model</i>	44
	3.3.2 <i>Retrieval Approach</i>	46
	3.3.3 <i>Retrieval Error Diagnostics</i>	47
	3.4 Results	52
	3.4.1 <i>Sensitivity to Cloud Fraction</i>	52
	3.4.2 <i>Sensitivity to Rainwater</i>	54
	3.4.3 <i>Warm Rain Cloud Results</i>	56
	3.5 Discussion	62
4	Interactions Between Warm Rain Clouds and Atmospheric Preconditioning in Tropical Disturbances	65
	4.1 Introduction	65
	4.2 Data	69

4.2.1	<i>Precipitation Data</i>	70
4.2.2	<i>Thermodynamic Properties</i>	71
4.2.3	<i>Precipitating Cloud LWP</i>	72
4.3	TD Identification	74
4.4	Results	75
4.4.1	<i>KWAJ</i>	75
4.4.2	<i>CPAC</i>	79
4.4.3	<i>TEPPS</i>	82
4.4.4	<i>Influence of SST</i>	85
4.5	Summary	89
5	Conclusions	95
	References	101

LIST OF TABLES

<u>Table</u>		<u>Page</u>
2.1	TMI instrument characteristics.	12
3.1	Forward model error sources (in K) for each TMI channel due to assumptions in SST (σ_{SST}), water vapor scale height (σ_{SCLHT}), temperature lapse rate (σ_{LR}), and cloud height (σ_{CLDHT}).	48
3.2	Forward model error sources (in K) for each TMI channel due to brightness temperature deconvolution (σ_{BG}), assumed cloud fraction errors (σ_{FCLD}), errors in PR rainwater estimates and assumed DSD (σ_{RW}).	49

LIST OF FIGURES

<u>Figure</u>	<u>Page</u>
2.1 Retrieval parameters, (a) LWP (g m^{-2}), (b) TPW (mm), (c) wind speed (m s^{-1}), and (d) χ^2 , for TMI T_{BS} at their native resolution (non-deconvolved) plotted against retrieval parameters from deconvolved TMI T_{BS} .	16
2.2 Retrieval parameters, (a) LWP (g m^{-2}), and (b) wind speed (m s^{-1}) for TMI T_{BS} at their native resolution (non-deconvolved) plotted against retrieval parameters from deconvolved TMI T_{BS} as a function of cloud fraction.	18
2.3 Percent difference in retrieved parameters (native resolution minus deconvolved) for (a) LWP, and (b) wind speed, as a function of cloud fraction.	19
2.4 Frequency of occurrence of cloud LWP (g m^{-2}) retrieved with (a) native resolution T_{BS} , (b) deconvolved T_{BS} , and for (c) ‘truth’ LWP assumed in T_{B} simulations.	22
2.5 Difference in the 85-GHz FOV cloud fraction and the 19-GHz FOV cloud fraction plotted against the percent difference in native resolution LWP retrieval and deconvolved LWP retrieval.	23
2.6 Cloud LWP and (a) 85-GHz horizontal polarization T_{BS} and (b) 85-GHz vertical polarization T_{BS} .	23
2.7 Deconvolved retrievals of (a) LWP and (b) wind speed plotted against retrievals of LWP using all native resolution T_{BS} .	24
2.8 Deconvolved retrievals of LWP and wind plotted against retrievals of LWP using (a,b) native resolution T_{BS} with 10-GHz deconvolved T_{B} substitution, (c,d) native resolution T_{BS} with 37-GHz deconvolved T_{B} substitution, (e,f) native resolution T_{BS} with 85-GHz deconvolved T_{B} substitution.	25

2.9	Deconvolved retrievals of LWP and wind plotted against retrievals of LWP using (a,b) native resolution T_{BS} with 37- and 85-GHz deconvolved T_B substitution, and (c,d) native resolution T_{BS} with 10-, 37-, and 85-GHz deconvolved T_B substitution.	27
2.10	$1^\circ \times 1^\circ$ LWP (g m^{-2}) retrieved with native resolution TMI T_{BS} plotted against $1^\circ \times 1^\circ$ LWP retrieved with deconvolved TMI T_{BS} averaged for (a) each swath, and (b) monthly.	29
2.11	(a) TMI retrieved LWP (g m^{-2}) and (b) synthetic LWP retrievals from native resolution (non-deconvolved) T_{BS} plotted against retrieval parameters from deconvolved T_{BS} without 85-GHz channels.	30
3.1	Mean LWP (g m^{-2}) with SST (K) for non-raining warm clouds for (a) MODIS and (b) AMSR-E and for raining warm clouds for (c) MODIS and (d) AMSR-E.	37
3.2	PR attenuation-corrected radar reflectivity (dBZ) with rainwater content (kg m^{-3}).	50
3.3	Difference in parameters, (a) LWP (g m^{-2}), (b) TPW (mm), (c) wind speed (m s^{-1}), and (d) χ^2 , retrieved with and without cloud fraction plotted against VIRS cloud fraction.	53
3.4	TMI OE-retrieved parameters (a) LWP (g m^{-2}), (b) TPW (mm), (c) wind speed (m s^{-1}), and (d) χ^2 , with and without PR rainwater estimates.	55
3.5	Portion of TRMM swath containing warm rain clouds with the VIRS infrared T_B (K) in (a), PR rain rate (mm hr^{-1}) in (b), optimal estimation LWP (g m^{-2}) retrieval without PR rain water estimation in (c), and optimal estimation LWP (g m^{-2}) retrieval using PR rainwater estimate in (d).	57
3.6	Mean TMI OE-retrieved LWP (g m^{-2}) with SST (K) for (a) non-raining warm clouds and for (b) raining warm clouds.	58
3.7	Ratio of mean TMI OE-retrieved LWP to PR-estimated rainwater plotted against SST (K).	60
4.1	GOES-10 visible albedo on 14 July 2000, where TDs are identified at both the TEPPS (T) and CPAC (C) locations.	76

4.2	ERA-40 anomalies in (a) temperature (K), (b) specific humidity (kg kg^{-1}), and (c) vertical velocity (m s^{-1}) at KWAJ (167.5°E , 7.5°N).	77
4.3	(a) Cloud LWP anomaly (g m^{-2}) and (b) CAPE anomaly (J kg^{-1}) composites for TD events at KWAJ (167.5°E , 7.5°N).	78
4.4	Composite of the anomaly in ratio of cloud LWP to rainwater for precipitating clouds for TD events at KWAJ (167.5°E , 7.5°N).	79
4.5	ERA-40 anomalies in (a) temperature (K), (b) specific humidity (kg kg^{-1}), and (c) vertical velocity (m s^{-1}) at CPAC (140.5°W , 7.5°N).	80
4.6	(a) Cloud LWP anomaly (g m^{-2}) and (b) CAPE anomaly (J kg^{-1}) composites for TD events at CPAC (140.5°W , 7.5°N).	81
4.7	ERA-40 anomalies in (a) temperature (K), (b) specific humidity (kg kg^{-1}), and (c) vertical velocity (m s^{-1}) at TEPPS (124.5°E , 7.5°N).	83
4.8	(a) Cloud LWP anomaly (g m^{-2}) and (b) CAPE anomaly (J kg^{-1}) composites for TD events at TEPPS (124.5°W , 7.5°N).	84
4.9	Cloud LWP anomalies (g m^{-2}) composited for (a) KWAJ, (b) CPAC, and (c) TEPPS, and CAPE (J kg^{-1}) composites at (d) KWAJ, (e) CPAC, and (f) TEPPS separated by high and low mean SSTs.	86
4.10	Mean rain rate (mm hr^{-1}) composites for high and low SST TD events at (a) KWAJ, (b) CPAC, and (c) TEPPS.	90
4.11	Zonal wind anomalies (m s^{-1}) for TD events with (a) low SSTs and (b) high SSTs.	91

LIST OF ACRONYMS

AMSR-E	Advanced Microwave Scanning Radiometer
BFE	Beam-filling Effect
BG	Backus and Gilbert (1970)
CAPE	Convective Available Potential Energy
CPAC	Location in central Pacific at 7.5°N, 140.5°W
DSD	Drop Size Distribution
ECMWF	European Centre for Medium-Range Weather Forecasting
ERA-40	European Centre for Medium-Range Weather Forecasting Reanalysis
ESMR	Electronically Scanned Microwave Radiometer
FOV	Field of View
GCM	Global Climate Model/General Circulation Model
GPCP	Global Precipitation Climatology Project
GPM	Global Precipitation Measurement Mission
IGRA	Integrated Global Radiosonde Archive
IPCC	Intergovernmental Panel on Climate Change
KWAJ	Location near Kwajalein at approximately 7.5°N, 167.5°E
LWC	Liquid Water Content
LWP	Liquid Water Path

MJO	Madden-Julian Oscillation
MODIS	Moderate Resolution Imaging Spectroradiometer
NIR	Near-Infrared
OE	Optimal Estimation
PR	Precipitation Radar
RSS	Remote Sensing Systems
SSM/I	Special Sensor Microwave/Imager
SST	Sea Surface Temperature
T_B	Brightness Temperature
TD	Tropical Depression-Type Disturbance
TEPPS	Location in the Tropical Eastern Pacific Process Study region at 7.5°N, 124.5°W
TIROS	Television Infrared Observation Satellite
TMI	TRMM Microwave Imager
TOGA-COARE	Tropical Ocean Global Atmosphere Coupled Ocean–Atmosphere Response Experiment
TPW	Total Precipitable Water
TRMM	Tropical Rainfall Measuring Mission
VIRS	Visible Infrared Scanner

Chapter 1

Introduction

1.1 Motivation

In the most recent assessment report by the Fourth Intergovernmental Panel on Climate Change (IPCC 2007), cloud feedback effects were reported to be the largest contributor to model differences in climate sensitivity estimates. Unraveling cloud feedback effect on the climate system is extremely difficult because of the complicated interactions between large-scale dynamics and small-scale changes in temperature, humidity, clouds, and precipitation. Because the warm SSTs in the tropical Pacific provide the necessary energy for deep convection, this region is often studied in attempts to assess cloud feedback effects. However, convective clouds produce competing positive and negative feedbacks on the climate system. Positive feedbacks occur when the clouds trap outgoing longwave radiation and negative feedbacks occur in the shortwave where clouds reflect incoming shortwave radiation. The strength and sign of feedback effects are highly dependent on the cloud properties. To complicate this, studies have shown that precipitation may play an important role in determining the properties of warm clouds. Therefore, changes to the rate at which cloud is converted to

precipitation with temperature may be extremely important to understanding shortwave cloud feedback effects.

1.2 Warm Rain Clouds

A substantial fraction of tropical convection is ‘warm’ clouds whose cloud top temperatures are below 273 K. Because of their strong reflection of solar radiation back to space, warm clouds mostly affect the shortwave portion of the radiation spectrum. In the longwave, these clouds absorb and re-emit the radiation at temperatures near that of the earth’s surface, so they have less effect. Some of these warm clouds do precipitate and the dominant process by which precipitation forms is through collision and coalescence. Particles within the cloud begin to grow by condensation to a radius of about 20 μm , after which the collision efficiencies become large enough for the particle to experience rapid growth. This growth is influenced by a number of factors such as the cloud water content and the updraft velocity. In an enhanced SST scenario, the Clausius-Clapeyron equation shows that an increase in temperature leads to an increase in water vapor. An increase in water vapor provides more available water for particle growth. Sun and Lindzen (1993) used a simple Bowen continuous growth model to show that particles grow 15% faster with an increase in surface temperature of 2 K assuming a constant updraft speed. Studies have also shown that an increase in SST results in enhanced vertical motion. Del Genio et al. (2005) also used a simple conceptual model to show that clouds below the freezing level form precipitation more efficiently at higher SSTs and at higher updraft speeds. These studies suggest that as the surface temperature increases, both updraft speed and water vapor increases, resulting in enhanced collision

and coalescence, which leads to greater precipitation formation. How this more efficient precipitation process affects the cloud remains a question of scientific study. Does the increase in water vapor result in the formation of enough cloud water to balance increased precipitation efficiency, so that the net cloud to rain ratio remains unchanged or does one process dominate the other? This is an important question and has substantial implications for warm rain clouds' radiative effects.

Another important process that is affected by warm, precipitating clouds is atmospheric preconditioning for deep convection. These clouds are responsible for some of the transport of heat and moisture to the lower and middle-troposphere that helps to destabilize the atmosphere enough for deep convection form. What role the variability in the properties of warm rain clouds has in atmospheric preconditioning prior to deep convection remains a fundamental outstanding question.

1.3 Cloud Property Retrievals

Retrievals of cloud properties from satellite remote sensing are one of the tools frequently employed to answer questions regarding the variability in cloud microphysical and radiative properties. Cloud property retrievals from optical and microwave satellite measurements have a long history dating back to the 1960's. Using a single infrared sensor, scientists were first able to observe the temperature of the clouds and infer the height of the cloud tops from the Television Infrared Observation Satellite (TIROS) series. Beginning with the Electronically Scanned Microwave Radiometer (ESMR) onboard the Nimbus-5 satellite, microwave observations have been used to retrieve cloud water and precipitation. Today, there are many complicated algorithms for the retrieval

of cloud properties from both visible and microwave radiation, however, the underlying principles of each type of retrieval are the same.

Retrievals of cloud properties from visible and near infrared (NIR) wavelengths operate on the principle that reflected solar radiation is dependent on the cloud's optical depth and mean particle size. At visible wavelengths, where there is little absorption of the radiation by the cloud droplets, the cloud's reflectance is mostly a function of optical depth. For NIR wavelengths where water vapor absorption is small, the cloud's reflectance is primarily dependent on the particle size. Theoretical radiative transfer calculations for reflection at visible and NIR wavelengths are performed over a variety of optical depth and particle sizes, as well as at a number of solar zenith and viewing zenith and azimuth angles. Given a set of visible and NIR observations, the optical depth and mean particle radius can be retrieved. Another important parameter that is related to the cloud optical depth and particle radius is the liquid water path (LWP) of the cloud. At visible wavelengths where the size parameter is large, i.e., the wavelength is small compared to the particle size, the extinction efficiency has a value of approximately 2 and the relationship between LWP, optical depth, and particle radius can be simplified as

$$LWP \approx \frac{2}{3} \rho_l r_e \tau \quad (1.1)$$

where ρ_l is the density of water, r_e is the particle effective radius, and τ is the optical depth.

Utilizing emitted microwave radiation is another method for the retrieval of cloud, precipitation, and atmospheric properties. In the absence of scattering by ice, measured microwave brightness temperatures are directly related to the absorption and emission by

the water content in the atmosphere, in the form of clouds, precipitation, and water vapor.

The cloud optical depth is just the integrated absorption due to the cloud water

$$\tau = \int_0^{z'} \left(\int_0^\infty Q_a n(r) \pi r^2 dr \right) dz \quad (1.2)$$

where Q_a is the absorption efficiency, r is the cloud particle size, and $n(r)$ is the number of particles of size, r . The absorption efficiency is proportional to the particle size,

$$Q_a = C_1 r \quad (1.3)$$

where C_1 is assumed to be approximately constant and contains terms representing the imaginary index of refraction of liquid water and the wavelength. The liquid water content, LWC, in the clouds is defined as

$$LWC = \frac{4}{3} \pi \rho_l \int_0^\infty n(r) r^3 dr \quad (1.4)$$

Substituting 1.3 and 1.4 into 1.2 yields,

$$\tau = \int_0^{z'} \left(C_1 \int_0^\infty n(r) \pi r^3 dr \right) dz = C_2 \int_0^{z'} LWC dz = C_2 LWP \quad (1.5)$$

where the LWP is just the vertically integrated LWC and the constant C_2 contains C_1 and the other constants from Eq. (1.4). Therefore, a retrieval scheme for LWP can be developed that is based on the physics of microwave radiative transfer. In physical retrieval schemes, a forward radiative transfer model is used to simulate microwave

brightness temperatures. The forward model is inverted to retrieve the solutions for the parameters of interest, in this case cloud LWP, total precipitable water, and wind speed that yield simulated brightness temperatures that agree with the measured brightness temperatures.

Both the instruments and the retrieval techniques have evolved and there are numerous optical and microwave retrievals of cloud properties and precipitation readily available to examine the properties of clouds in the Tropics. However, comparison of some of the most advanced products show discrepancies when the clouds are raining due to their limitations. Part of the work presented in this dissertation is aimed at addressing these discrepancies to study the LWP of clouds when they are precipitating.

1.4 Current Study

The work presented in this dissertation is aimed at understanding the role that warm rain systems play in the Tropics. One of the main goals of this work is to explore the role of the precipitation process in determining the liquid water content of warm rain clouds. However, to understand warm rain systems, a better representation of their properties is required. A retrieval algorithm for the study of cloud LWP of warm, precipitating clouds has been developed. To overcome the limitations of microwave or optical only retrievals of LWP in precipitating clouds, microwave, optical, and precipitation radar measurements are combined. Using information provided by the optical sensor and precipitation radar, the microwave measurements can be used to retrieve LWP associated with the cloud water content even when the clouds are precipitating.

The method for the inversion of microwave observations to retrieve cloud properties utilized in this study is the optimal estimation approach. Optimal estimation provides a framework to combining measurements, a forward model, and some a priori knowledge about the atmospheric state to retrieve cloud and atmospheric properties. It also allows for consideration of the uncertainties in the measurements, model, and assumptions made within the algorithm. This work builds on a previous algorithm developed by Elsaesser and Kummerow (2008) for the retrieval of parameters from non-raining oceanic clouds. Because we are retrieving in raining scenes, a number of modifications must be made to the existing algorithm. The microwave observations are first deconvolved to a common resolution following the methods of Backus and Gilbert (1970). This resampling of the observations to a common field of view (FOV) is necessary because the retrieval also utilizes information from an optical instrument to define the cloud fraction within the microwave FOV. By using the visible and infrared channels as a cloud mask to calculate the cloud fraction within the footprint, we can account for some of the scene inhomogeneities due to the microwave instrument sampling both clear and cloudy scenes within the same FOV. The retrieval algorithm also uses rainfall estimates from precipitation radar to calculate the contribution of rainwater's emission and scattering to the microwave brightness temperatures, so that the retrieval need only find the solution for the total precipitable water and cloud LWP that accounts for the rest of the emission and scattering.

The work from this study is separated into three chapters, which are written as independent papers. Understanding the sensitivities of the retrieval algorithm is very important to interpreting the results. The sensitivity of the retrieval to the addition of

deconvolved TMI brightness temperatures and the resultant beam-filling effects are presented in Chapter 2. Chapter 3 describes the retrieval algorithm and investigates the cloud fraction and rainwater sensitivities in the retrieval. Chapter 3 also explores the suggestion that precipitation increases occur at the expense of cloud water at higher SSTs. The retrieval algorithm described in Chapter 3 has many important applications. Another main goal of this work is to study the link between warm rain clouds and the preconditioning of the lower and middle troposphere for deep convection. The relationship between the properties of precipitating warm clouds and moistening and heating in the lower and middle troposphere is examined for tropical depression-type disturbances across the Pacific Ocean in Chapter 4. Finally, a summary of the dissertation is presented in Chapter 5.

Chapter 2

On the Consequences of Resampling Microwave Radiometer Measurements for Use in Retrieval Algorithms

2.1 Introduction

Because of the single antenna used in making measurements at different microwave frequencies, the spatial resolution of the measurements varies with the frequency. However, use of microwave measurements at a common resolution in multi-frequency retrievals of atmospheric parameters is often desirable and sometimes necessary. Data deconvolution has a long history of use in earth sciences. Backus and Gilbert (1970; hereafter BG) described a technique for inverting seismic data to retrieve Earth density profiles. This approach was first applied to resolution modification of satellite radiometer measurements by Stogryn (1978) and is now commonly used to resample data to a common resolution from microwave radiometer measurements observed by satellites. The BG approach to microwave radiometer measurement enhancement takes advantage of the overlapping antenna patterns by combining nearby measurements to increase the resolution. Retrievals of cloud water and rainfall are

commonly performed both with and without resampled microwave measurements. These retrievals are often used as comparisons or validation for one another and usually try to overcome beam-filling effects due to resolution differences by averaging the two retrievals to a common lower spatial resolution. The beam-filling effect, or the effect of partially cloud or rain-filled field of view (FOV) on the sampled microwave brightness temperatures (T_B), has been documented by several studies for both clouds (e.g., Melitta and Katsaros 1995; Greenwald et al. 1997, Bremen et al. 2002) and rainfall (e.g., Chiu et al. 1990; Short and North 1990; Kummerow 1998). Microwave instruments typically have large FOVs, which may contain both clear and cloudy areas. The sensor integrates over the entire scene to measure the radiance and compute the brightness temperature associated with that FOV. For an FOV with clear and cloudy areas, the radiance measured at the satellite and the resulting brightness temperature would be less than that for a completely cloud-filled scene and is known as the beam-filling effect (hereafter, BFE). The BFE is caused by the nonlinear relationship between microwave brightness temperatures and LWP or rain. Microwave T_B s are an exponential function of LWP and rain. The concave shape of the exponential relationship always causes an underestimate in the T_B if the parameter is not homogeneous, which can mean either a partially cloud-filled FOV or completely cloud-filled FOV with an inhomogeneous distribution of LWP. This was demonstrated mathematically for rainfall in Appendix B of Graves (1993), however, the same is true for LWP. A number of studies have illustrated the BFE in LWP retrievals using microwave satellite data. Melitta and Katsaros (1995) combined passive microwave data from Special Sensor Microwave/Imager (SSM/I) with visible and infrared data to identify the BFEs at 37- and 85-GHz. They found that with decreasing

cloud fraction, lower microwave cloud liquid water path is retrieved at both 37 and 85 GHz channels. Greenwald et al. (1997) quantified the BFE at 37 GHz using independent microwave and solar reflectance retrievals of LWP and computed a 22% reduction in microwave LWP for an average cloud fraction of 73%. The reduction in retrieved microwave LWP at lower cloud fractions, i.e., more inhomogeneity, shown in these two studies is consistent with the underestimate in T_{BS} due to BFEs. These studies examining the cloud LWP BFE focused on the comparing higher resolution retrievals from an independent method, such as visible/near-infrared retrievals, with the lower resolution microwave LWP retrieval. Comparing retrievals of the same dataset, where one is performed on the microwave measurements at their sampled native resolution and another is performed on the same data that has been resampled to a common resolution, shows that inhomogeneity effects are still very large. In this paper, we examine the consequences of data deconvolution on an optimal estimation retrieval algorithm that uses microwave radiometer measurements to retrieve cloud LWP, wind speed, and total precipitable water (TPW). Results show that data deconvolution has a substantial effect on the retrieved parameters when compared with retrievals performed on microwave radiometer observations at their native resolution due to BFEs. These effects will be seen to correspond to the intrinsic variability of the parameter within the FOV and are not eliminated by averaging two retrievals performed on different resolutions to a common spatial grid.

2.2 Deconvolution Method

The microwave radiometer dataset employed in this study is from the TRMM

TMI. The TMI is a conically scanning passive microwave radiometer with nine channels, summarized in Table 2.1. The resolution is diffraction limited and thus ranges from roughly 60 km at 10 GHz to 7 km at 85 GHz. More information regarding the instrument characteristics can be found in Kummerow et al. (1998).

The TMI T_{BS} are deconvolved to a common FOV corresponding to the horizontally polarized 19-GHz FOV using the BG as applied to the SSM/I sensor by Robinson et al. (1992). The method uses the spatial overlap of the antenna gain function of adjacent pixels in order to reconstruct the T_B as it would be observed by a radiometer with any desired gain function. In this work the desired gain function is that of the 19-GHz channel. The data could be resampled to a higher resolution, however, the associated noise becomes larger. The enhancement of the 10-GHz channel to the 19-GHz FOV increased the noise level from 0.54 K to about 1.5 K, which was deemed acceptable. Trying to increase the resolution of the 10-GHz channel to that of the 37-GHz FOV would increase the noise to approximately 12.5 K, which could significantly affect the retrieval.

The observed brightness temperatures, T_N , at location, (x, y) , are given by,

$$T_N(x, y) = \int T_B(x, y) G_i dx dy \quad (2.1)$$

Table 2.1 TMI instrument characteristics.

Channel	1	2	3	4	5	6	7	8	9
Frequency	10.65	10.65	19.35	19.35	21.3	37.0	37.0	85.5	85.5
Polarization	V	H	V	H	V	V	H	V	H
FOV-Down track (km)	59.0	60.1	30.5	30.1	27.2	16.0	16.0	6.7	6.9
FOV-Cross track (km)	35.7	36.4	18.4	18.2	16.5	9.7	9.7	4.1	4.2

where $T_B(x,y)$ is the actual scene brightness temperature and $G_i(x,y)$ is the antenna response function for observation i . Application of the deconvolution method to the TMI data to compute the effective brightness temperature, T_{BG} , at the resolution of the 19-GHz channel is constructed by using a linear combination of nearby observations. This is expressed as,

$$T_{BG}(x,y) = \sum_{i=1}^N a_i T_N(x,y) = \int \left(\sum_{i=1}^N a_i G_i(x,y) \right) T_B(x,y) dx dy \quad (2.2)$$

where, a_i , are coefficients that must be computed for each channel and scan position. These calculations are time consuming, but because the TMI antenna patterns and scan geometry are known and fixed, the coefficients only need to be calculated once and can then simply be applied to each orbit. We chose to use an 11 x 11 array of pixels surrounding the pixel to be deconvolved leading to a value of $N = 121$.

Because the antenna temperature measurement uncertainties are uncorrelated, standard propagation of errors provides the variance in the deconvolved T_B s as,

$$e^2 = (\Delta T_{rms})^2 \sum_{i=1}^N a_i^2 \quad (2.3)$$

where ΔT_{rms} is the uncertainty in the observed antenna temperatures. Due to this inherent uncertainty, the deconvolution technique requires a balance between resolution enhancement and amplification of noise. Therefore, following Robinson et al. (1992) we minimize the function,

$$Q = Q_0 \cos(\gamma) + e^2 w \sin(\gamma), \quad (2.4)$$

where the first term on the right hand side represents resolution enhancement and the second term represents the propagation of noise. The weighting between these terms is given by γ , which may vary between 0° and 90° . Here w is a scale factor with units of K^{-2} used to make the two terms on the right hand side of Eq. (2.4) dimensionally and numerically similar. As discussed by Stogryn (1978) the exact value of w chosen does not change the physical content of the theory and in this work the constant value of $w = 10^{-12} \text{K}^{-2}$ is found to be appropriate.

In the case of the 21-, 37-, and 85-GHz channels the resolution is being degraded to that of the 19-GHz FOV. This is an averaging process, which naturally reduces error. As a result, amplification of noise is not a concern and we set $\gamma = 0$ when computing the deconvolution coefficients for these channels. In the case of the 10-GHz channels, the resolution is enhanced and proper care must be taken to choose γ carefully so as to minimize the amplification of noise. Through trial and error we find an appropriate value of γ to be 85° , which heavily emphasizes the minimization of noise amplification while matching the resolution to 19-GHz FOV.

After minimizing Eq. (2.4) to solve for the coefficients, a_i , they are applied to each TMI pixel to calculate T_{BG} . These resampled TMI T_{BS} are then used as input to the optimal estimation (OE) retrieval algorithm described briefly in the following section and the resultant changes in retrieved quantities due to deconvolution and their associated BFEs are analyzed.

2.3 Retrieval and Results

The algorithm used in this paper to illustrate the effects of data deconvolution was first developed by Elsaesser and Kummerow (2008) for the retrieval of non-raining parameters over oceans and used passive microwave radiometer observations at their native resolution. Further development of this algorithm attempted to address scene inhomogeneities by accounting for both clear and cloudy areas within the TMI footprints by calculating cloud fraction from visible and infrared datasets. To define a cloud fraction over a given area required that the microwave measurements at the different frequencies be resampled to a common resolution. The BG method was applied to deconvolve the data to the resolution of the 19-GHz FOV as discussed in the previous section and the retrieval was run on both the native-resolution TMI measurements and the resampled TMI measurements. The differences between the retrievals are examined and the BFEs are assessed.

Resampling the TMI data to the resolution of the 19-GHz FOV had a larger impact on the retrieval than expected. Figures 2.1a-d are a comparison of the TMI OE retrieval parameters at the native resolution of each TMI channel and the TMI OE retrieval deconvolved to the resolution of the 19-GHz channel for three months of data (December 2005 - February 2006) in the tropical western Pacific from 30°S – 30°N, 130°E – 170°W. Figures 2.1a-c show that the deconvolution of the data has little effect on the retrieved TPW, however it results in a decrease in the retrieved LWP of about 30%. The wind speed from the retrieval with the deconvolved data tends to consistently be 1 m s⁻¹ higher up to wind speeds of about 10 m s⁻¹ and up to 2 m s⁻¹ lower for wind speeds of 20 m s⁻¹. Though the scale of LWP in Figure 2.1a extends to 600 g m⁻² to

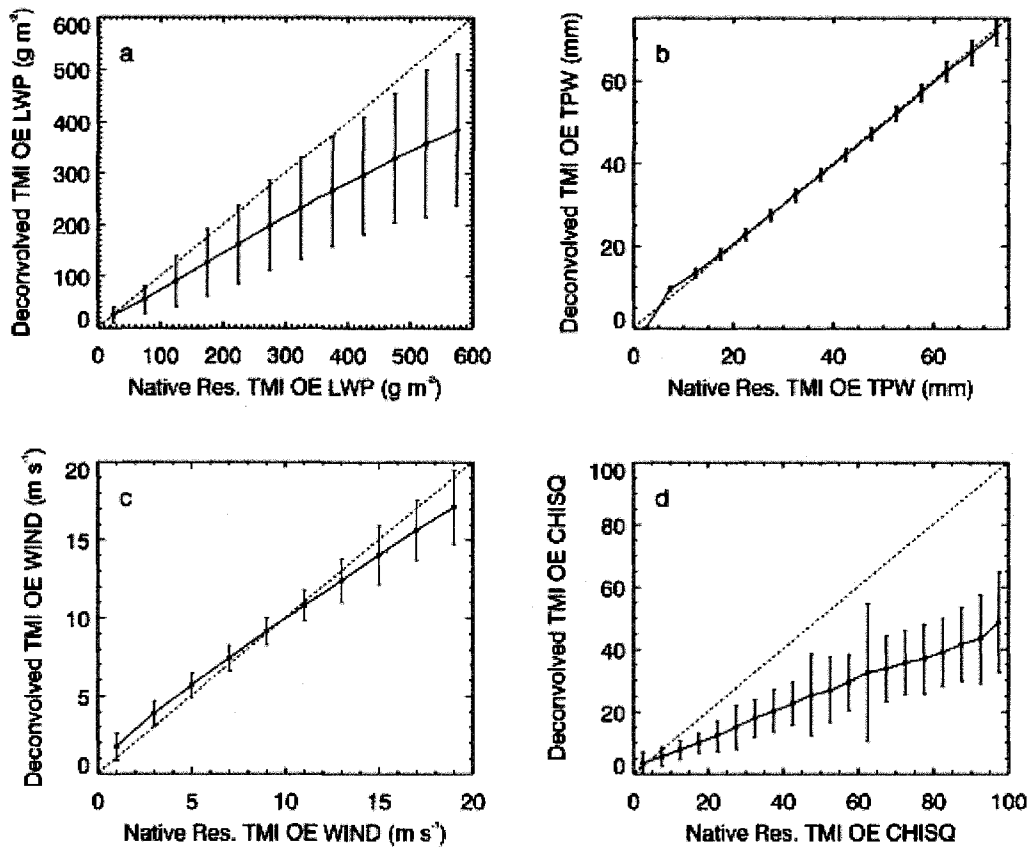


Figure 2.1 Retrieval parameters, (a) LWP (g m^{-2}), (b) TPW (mm), (c) wind speed (m s^{-1}), and (d) χ^2 , for TMI T_{BS} at their native resolution (non-deconvolved) plotted against retrieval parameters from deconvolved TMI T_{BS} .

illustrate that the LWP difference increases as LWP increases, it should be noted that the majority of the clouds have LWP values below 200 g m^{-2} . A useful diagnostic that results from optimal estimation retrievals is the χ^2 statistic shown in Figure 2.1d. The χ^2 value indicates how well the simulated T_{BS} in the forward model of the retrieval algorithm match the observed T_{BS} , therefore larger values of χ^2 suggest a poorer fit between simulated and measured T_{BS} than low values of χ^2 . One of the benefits of using deconvolved T_{BS} over native T_{BS} in the retrieval is the lowering of the χ^2 statistic, shown in Figure 2.1d, indicating that the resampled data results in a better fit retrieval solution than the native resolution retrieval. This is another example of scene inhomogeneity effects, since at the native resolution of the TMI dataset, the channels are sampling different scenes.

Because the TPW is relatively insensitive to resampling, only the differences in the retrieved LWP and wind speeds are examined as a function of the cloud fraction within the 19-GHz FOV. Figure 2.2 shows LWP and winds retrieved with native resolution and deconvolved TMI T_{BS} for different cloud fraction bins – 100% cloudy, greater than 75% cloudy, 50% to 75% cloudy, 25% to 50% cloudy, and less than 25% cloudy. This figure illustrates that as cloud fraction decreases, the systematic differences between the two retrievals increase. At cloud fractions greater than 75% the bias between the two retrievals ranges from 10% at low LWPs up to 35% at very high LWPs. For the lowest cloud fractions, the range in the bias is much larger, from 10% at low LWPs to almost 60% at high LWPs. The bias in the wind speed does not seem to be as large of a function of cloud fraction as the LWP, especially for wind speeds below 10 m s^{-1} . At the highest wind speeds, the bias does slightly increase with cloud fraction.

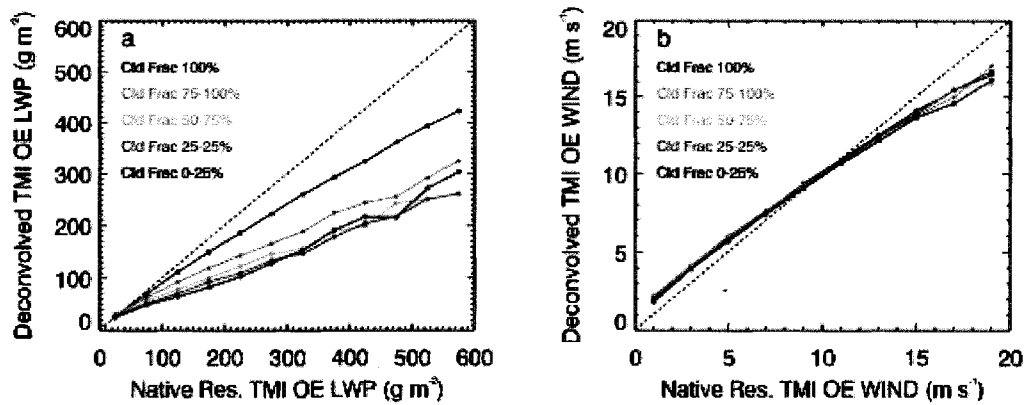


Figure 2.2 Retrieval parameters, (a) LWP (g m^{-2}), and (b) wind speed (m s^{-1}) for TMI T_{BS} at their native resolution (non-deconvolved) plotted against retrieval parameters from deconvolved TMI T_{BS} as a function of cloud fraction.

Figure 2.3 summarizes the difference in retrieved LWP and winds using native and deconvolved T_{BS} as a function of cloud fraction. The retrieval algorithm in this study uses both the 37- and 85-GHz channels to retrieve LWP, but results in Figure 2.3 are similar to those shown by Melitta and Katsaros (1995). The difference between the retrievals increases with decreasing cloud fraction and between 70-75% cloudy, we find a reduction in cloud LWP for resampled T_{B} retrievals of 20%, almost identical to that found by Greenwald et al. (1997). Above about 80% cloud fraction, the difference between retrieved LWP decreases substantially. As suggested in Figure 2.2, above cloud fractions of about 40%, the difference between the retrievals of wind speed does not substantially change with cloud fraction, with the native-resolution T_{BS} retrieving about 20% lower wind speed than the deconvolved T_{BS} .

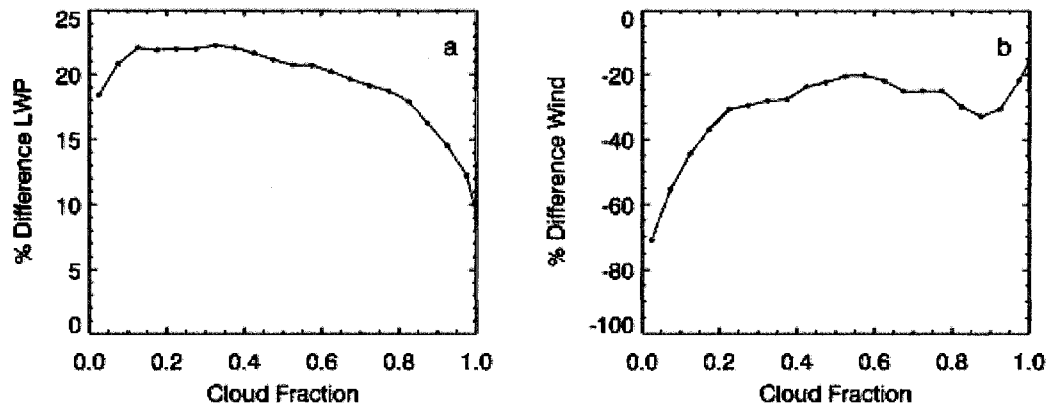


Figure 2.3 Percent difference in retrieved parameters (native resolution minus deconvolved) for, (a) LWP, and (b) wind speed, as a function of cloud fraction.

While there will still be scene inhomogeneities within the resampled data, by limiting the sample to only 100% cloud fraction, we have at least reduced the effects of sampling a combination of clear and cloudy scenes, although the cloud fraction effects are not fully accounted for in the non-deconvolved retrieval. Because the cloud fractions were calculated for the deconvolved data, the clouds are only guaranteed to completely fill the 19-GHz footprint. It is likely that some of the observed differences can be attributed to the clouds not completely filling the large 10-GHz footprint, which may explain some of the 10% difference in Figure 2.3 at 100% cloudy. Another factor contributing to the differences at 100% cloudy is the distribution of LWP within the FOV. Even at 100% cloud fraction, variability of LWP within the FOV will affect the retrieved results. These retrievals would only be expected to be the same if the cloud completely filled the 10-GHz footprint and the LWP was homogeneous across the entire scene.

2.4 Synthetic Tests

While we assume that beam-filling effects are responsible for these results, we test the effects of the deconvolution algorithm in a more controlled environment. A set of synthetic cloud scenes for a range of cloud LWP from 75 to 400 g m⁻² is created. Each scene is 200 x 200 km at a resolution of 1 x 1 km and contains from 10 – 75% cloud coverage, where the cloud locations in the scene are chosen by a random number generator. Because the locations of the clouds are chosen randomly, the cloud fraction of the entire scene is not necessarily representative of the scene sampled for our retrieval. Clouds are created to be 25 x 25 km and each cloud within the scene is randomly populated with LWP values that return the chosen mean cloud LWP (75, 100, 200, 300, or 400 g m⁻²) with a standard deviation of 30%. Despite the fact that the clouds are originally 25 x 25 km, because of the random selection of the locations, clouds often merge to create a scene with a population of cloud sizes.

For each 1 x 1 km pixel in the scene, we then run the forward model used in our retrieval with a prescribed 8 m s⁻¹ wind speed, TPW value of 24 mm, and SST of 293 K, along with either zero LWP if the pixel is clear sky or their assigned cloud LWP value, to calculate the associated microwave brightness temperatures at each channel. The brightness temperatures for each frequency are then sampled in the center of the scene at both the resolution of each microwave channel as observed by the TMI and at the resolution of the 19-GHz FOV as would be calculated from the BG deconvolution algorithm. Using these brightness temperatures, the optimal estimation retrieval algorithm is run and the results are compared. Histograms of the frequency of LWP values retrieved at their native resolution and at their resampled resolution are plotted in

Figure 2.4, as well as the ‘truth’ for mean LWP assigned for the calculation of the microwave T_{BS} . For the synthetic deconvolved LWP retrievals, the histogram shifts to the left toward lower values and the mean LWP retrieved for all scenes is about 33% higher in the native resolution retrievals. Figure 2.4 also shows that the histogram and mean LWP of deconvolved retrievals are more representative of the true mean LWP within the FOV than the native resolution retrieved LWP. Similar to the actual data, the synthetic results show that the retrieval using deconvolved T_{BS} on average results in a lower retrieved LWP and an approximately 15% higher retrieved wind speed. To illustrate the effects of beam filling on cloud LWP, we compare the difference in retrieved results with the difference in cloud fraction of the 85-GHz FOV at its native resolution and cloud fraction at the resampled 19-GHz FOV in Figure 2.5. This figure shows that the percent difference in cloud LWP is strongly correlated with the difference in cloud fraction between the smaller 85-GHz and larger 19-GHz FOV sizes. Also, the majority of the points are located at positive cloud fraction differences, indicating that when cloud fraction is high for the smaller footprints, there is a tendency to move towards lower cloud fraction when resampled to the larger 19-GHz FOV. The likely explanation for this is that as the size of the FOV increases, there is a higher likelihood of viewing some clear area within the scene. The reduction in retrieved LWP as the FOV size increases is due to the nonlinear nature between the T_{BS} and LWP that was previously described and is shown for the 85 GHz horizontally and vertically polarized channels in Figure 2.6. This bias in retrieved LWP is similar to the bias with FOV size shown by Graves (1993) and Ha and North (1995) for rainfall retrievals.

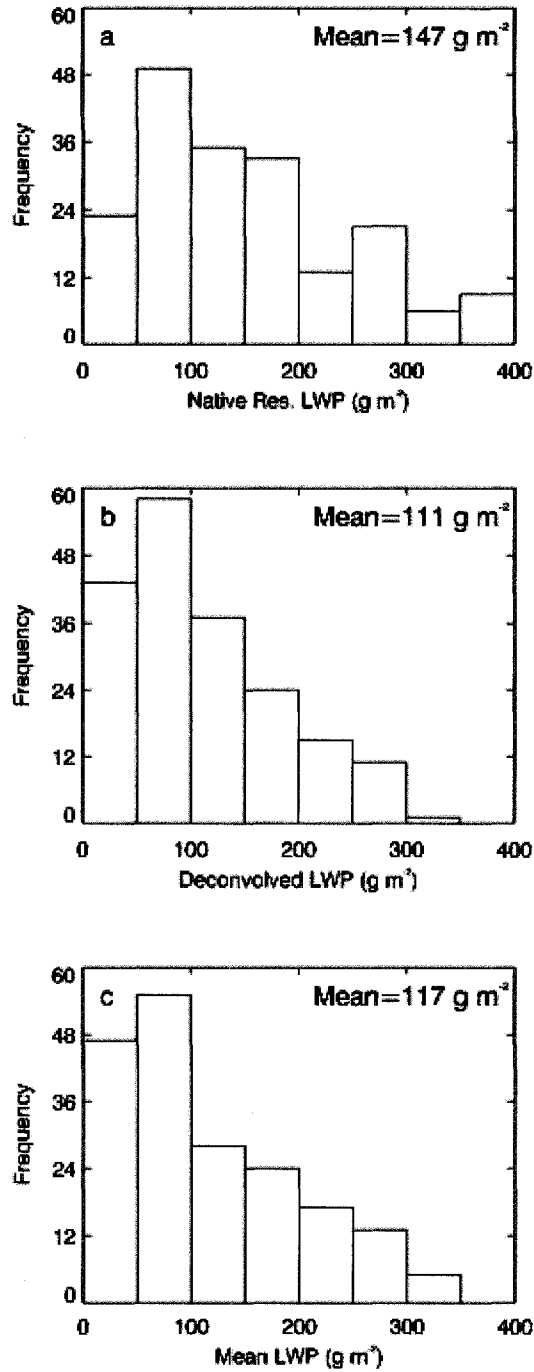


Figure 2.4 Frequency of occurrence of cloud LWP (g m⁻²) retrieved with (a) native resolution T_{BS}, (b) deconvolved T_{BS}, and for (c) ‘truth’ LWP assumed in T_B simulations.

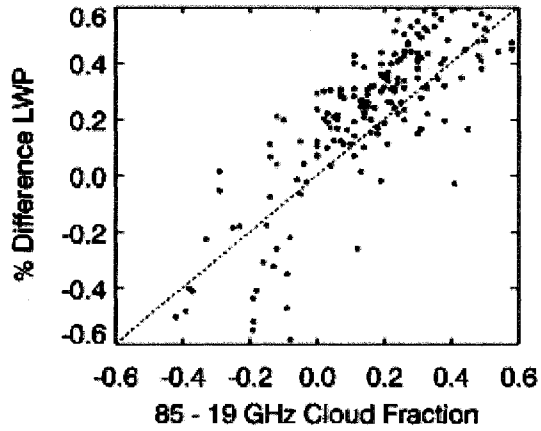


Figure 2.5 Difference in the 85-GHz FOV cloud fraction and the 19-GHz FOV cloud fraction plotted against the percent difference in native resolution LWP retrieval and deconvolved LWP retrieval.

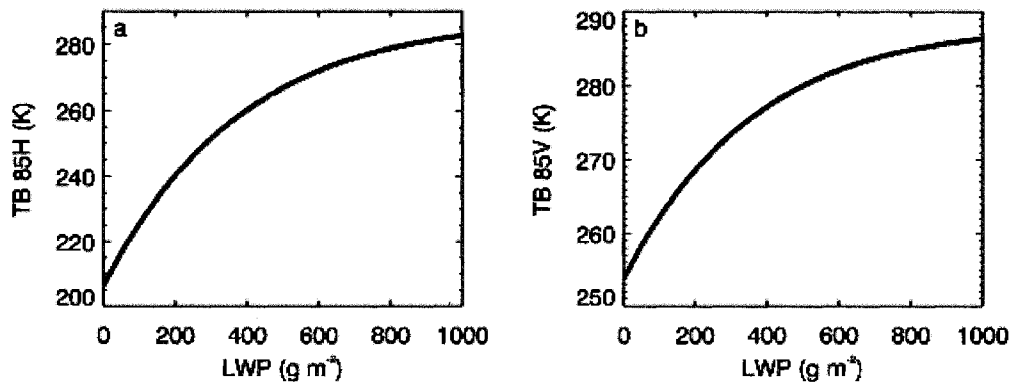


Figure 2.6 Cloud LWP and (a) 85-GHz horizontal polarization T_{BS} and (b) 85-GHz vertical polarization T_{BS} .

While these synthetic results clearly illustrate that BFEs are driving the differences between the native resolution and resampled retrievals, it is not yet clear which channels are most responsible for these differences. To examine this, we run several tests by substituting the 10-, 37- and 85-GHz deconvolved T_{BS} individually and in combination into the synthetic scenes where all other channels are run with their native TMI resolution T_{BS} . We omit the 19- and 21-GHz tests because the 19-GHz native-resolution and deconvolved T_{BS} are the same and the T_{BS} at 21 GHz are so close that it makes no difference in the retrieved parameters.

In the first test, we substitute only the 10-GHz deconvolved T_B in the retrieval. For reference, Figures 2.7a and 2.7b are the synthetic retrieval results with all the channels sampled at either their native resolution or deconvolved resolution. The deconvolved LWP and wind speed results are plotted against the native resolution results with the deconvolved 10-GHz T_B substitution in panels (a) and (b) of Figure 2.8. From these results, it is obvious that the 10-GHz channel provides little information for the

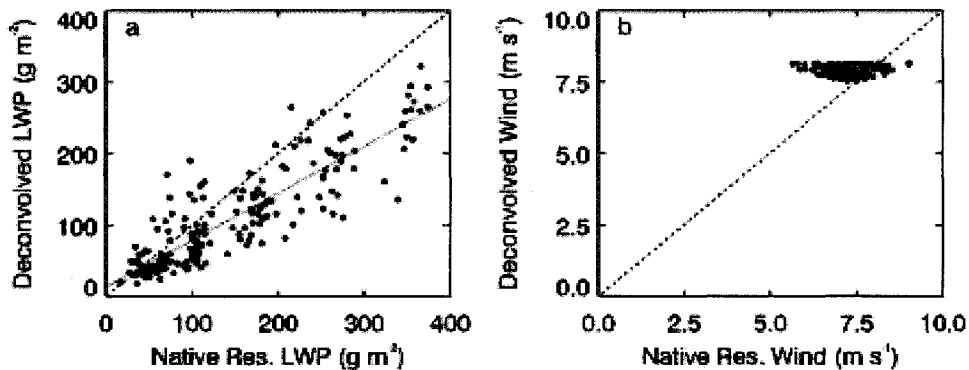


Figure 2.7 Deconvolved retrievals of (a) LWP and (b) wind speed plotted against retrievals of LWP using all native resolution T_{BS} .

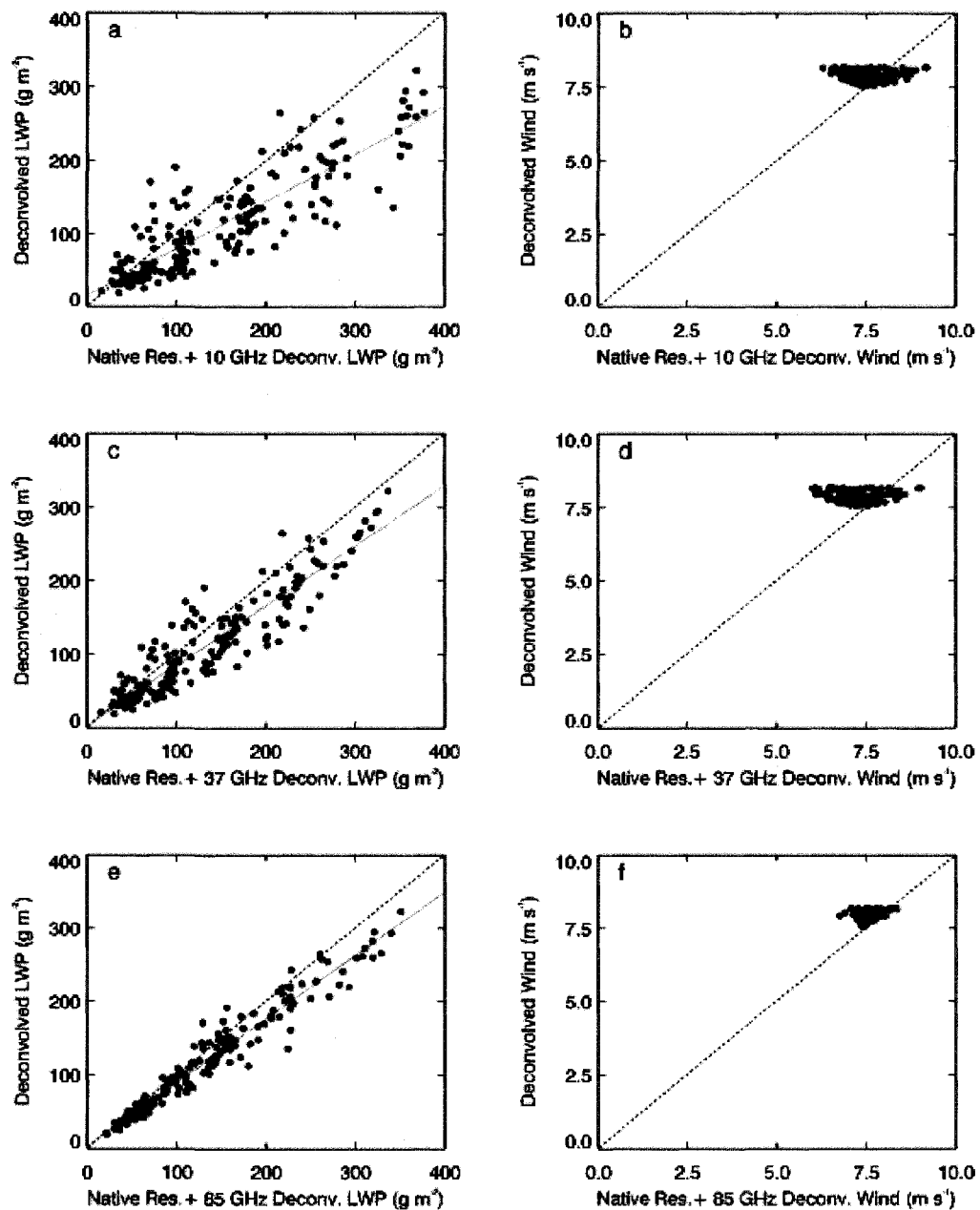


Figure 2.8 Deconvolved retrievals of LWP and wind plotted against retrievals of LWP using (a,b) native resolution T_B s with 10-GHz deconvolved T_B substitution, (c,d) native resolution T_B s with 37-GHz deconvolved T_B substitution, (e,f) native resolution T_B s with 85-GHz deconvolved T_B substitution.

cloud LWP, but it does result in an increase in the wind speed suggesting that the resampling of the low frequency channel is driving some of the change in retrieved wind speed. In the second and third tests we substitute the 37- and 85-GHz deconvolved T_{BS} with the other channels at their native resolutions. The 37- and 85-GHz results are shown in Figures 2.8c,d and 2.8e,f, respectively. It is clear that the resampling of the high frequency channels are responsible for the lower LWP being retrieved, though neither channel alone fully explains the discrepancy observed in Figure 2.7a. It is interesting to note the effect that resampling the 85-GHz channel has on the wind speed retrieval, which suggests that some of the increased wind speed in retrievals using deconvolved T_{BS} is actually a compensating effect that is produced as a by-product of retrieving the lower LWP.

In the next test, we substitute both the 37- and 85-GHz deconvolved T_{BS} , with the results shown in panels (a) and (b) of Figure 2.9. The LWP retrieval now retrieves the same solution as that with all of the channels resampled to the 19-GHz FOV and shows that the decrease in retrieved LWP using deconvolved brightness temperatures is fully explained by the high frequency channels. The 37- and 85-GHz channels are both being resampled to a resolution lower than their native resolution. While it is clearly scene dependent as shown by the scatter, Figure 2.5 showed that on average, moving from a higher resolution to lower resolution tends to reduce the cloud fraction, which lowers the emission signature and T_{BS} and thus, the retrieved LWP. These results also show that the difference in retrieved wind speed with resampled data cannot be fully explained by compensating effects within the retrieval. The final test (shown in Figures 2.9c,d), which adds the deconvolved 10-GHz T_{BS} to the previous test, yields the same results as the

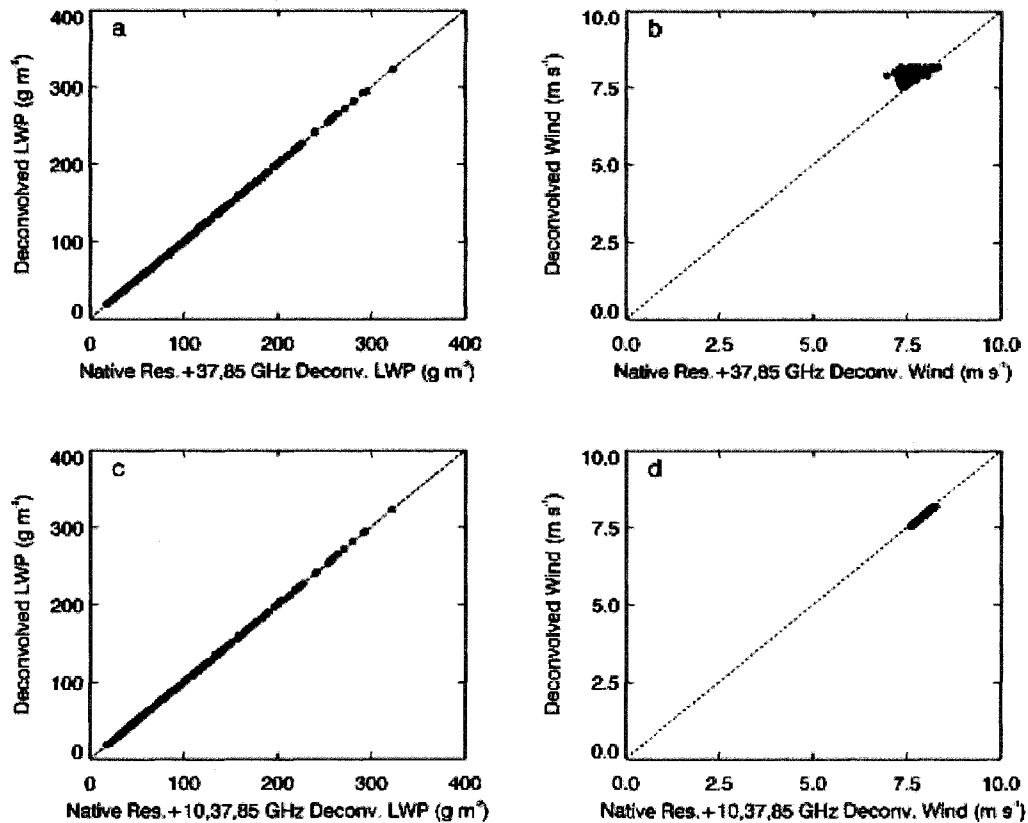


Figure 2.9 Deconvolved retrievals of LWP and wind plotted against retrievals of LWP using (a,b) native resolution T_B s with 37- and 85-GHz deconvolved T_B substitution, and (c,d) native resolution T_B s with 10-, 37-, and 85-GHz deconvolved T_B substitution.

retrieval run using all resampled T_B s. It also supports our previous test result that the high frequency channels are solely responsible for the decreased LWP and that the increased wind speed is a combination of compensating effects from the reduced LWP retrieved from the combination of deconvolved 37- and 85-GHz T_B s and the increase in speed due to the resampling of the 10-GHz channels.

To verify our tests on the real data, the optimal estimation retrieval algorithm was run with combinations of native resolution and deconvolved TMI brightness temperatures as in the fourth and fifth tests on our synthetic scene. While not shown here, the retrievals from the TMI data reproduced the results of our tests. Degrading the resolution of the 37- and 85-GHz frequencies resulted in consistently lower retrieved LWP with a compensating increase in wind speed. Enhancing the resolution of the 10-GHz frequencies did increase the wind speeds even more for wind speeds below 8 m s^{-1} , as in our synthetic tests, however, above 8 m s^{-1} the addition of the resampled 10-GHz data tended to decrease the wind speed.

As mentioned in the introduction, when comparing parameters that are retrieved at different resolutions, many users try to overcome resolution effects and BFEs by averaging the retrieved products, like LWP, to the lower resolution product or to a common resolution. Figure 2.10a shows the LWP from our two retrievals, one at the native TMI resolution and the other at the 19-GHz FOV resolution, averaged onto a $1^\circ \times 1^\circ$ grid for each swath. Averaging should account for spatial resolution differences, but any residual differences should be due to BFEs in the retrievals. While the bias is not as large as that shown in Figure 2.1, these results show that a significant bias of about 20% still exists between the LWP even after averaging. Greenwald et al. (1997) pointed out that BFEs are less of an issue when averaged over monthly timescales for large grid boxes. The deconvolved and native TMI resolution retrievals were averaged on a $1^\circ \times 1^\circ$ grid for a month of data and plotted in Figure 2.10b. While even more differences are resolved by such large space-time averaging, a residual bias of about 10% still exists. Again, because of the nonlinear nature of the relationship between T_{BS} and LWP,

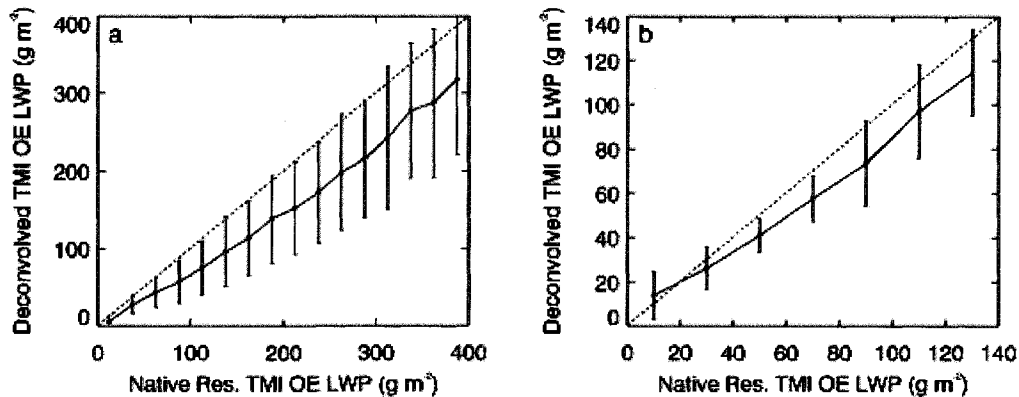


Figure 2.10 $1^\circ \times 1^\circ$ LWP (g m^{-2}) retrieved with native resolution TMI T_{BS} plotted against $1^\circ \times 1^\circ$ LWP retrieved with deconvolved TMI T_{BS} averaged for (a) each swath, and (b) monthly.

averaging in radiance space is not comparable to averaging in parameter space and cannot account for the beam-filling effects even in retrievals performed on the same dataset at different resolutions. These effects become very important in work that uses retrievals of LWP in climate studies or in tuning model parameters to reproduce observational results.

2.5 Retrieval without 85-GHz Channels

Since microwave retrievals of LWP are based on the emission from cloud water and the effects due to scattering increase with frequency, many microwave retrievals of LWP do not use the 85-GHz channels. The synthetic retrieval results showed that much of the difference in retrieved LWP between native resolution and resampled data can be attributed to the 85-GHz frequency. Figure 2.11a shows the results from the optimal estimation retrieval for LWP using native TMI resolution and deconvolved T_{BS} without

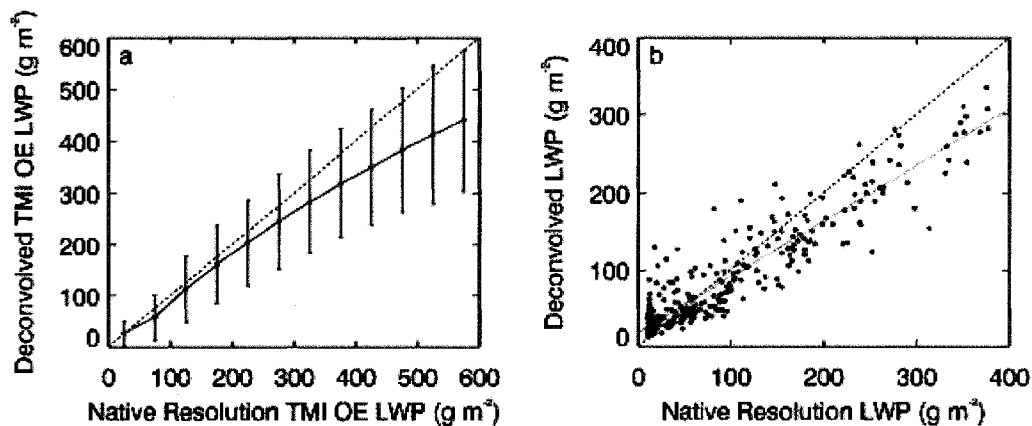


Figure 2.11 (a) TMI Retrieved LWP (g m^{-2}) and (b) synthetic LWP retrievals from native resolution (non-deconvolved) T_{BS} plotted against retrieval parameters from deconvolved T_{BS} without 85-GHz channels.

the 85-GHz channels. For values of LWP below 200 g m^{-2} the two retrievals agree very well, but above that the deconvolved TBs retrieve up to 20% lower LWP. Figure 2.11b shows the results for the synthetic scenes retrieved without the 85-GHz channels. Like the real data, the synthetic results show pretty good agreement for lower LWPs, but the differences increase up to about 25% as the LWP increases. These differences are smaller than that shown for the retrieval using the 85 GHz because the relationships between LWP and T_{BS} at the lower frequencies are not as nonlinear, so the BFEs are not as large. However, because the 37-GHz channel is being resampled to a larger FOV, some BFEs remain.

2.6 Discussion

Data deconvolution algorithms are commonly used to overcome the resolution differences inherent in satellite passive microwave remote sensing. We tested the effects

of data deconvolution in an optimal estimation microwave retrieval of LWP, TPW, and wind speed and found that beam-filling effects are substantial. Retrievals performed with TMI data as well as synthetic scenes show differences between retrieved LWP with native resolution and deconvolved T_{BS} up to about 30%, although this increases with decreasing cloud fraction and increasing LWP. Differences in the cloud fraction between the 85-GHz FOV and the resampled 19-GHz FOV are found to be highly related to the differences in retrieved LWP. Synthetic results show that resampling the 37- and 85-GHz channels to a lower resolution is responsible for the general decrease in LWP in the deconvolved retrievals, although the 85-GHz channels are the largest contributor. Synthetic results also indicate that the differences in wind speed retrieved with native resolution T_{BS} and deconvolved T_{BS} are due to a combination of resampling the 10-GHz channels and compensating effects of retrieving lower LWP solutions driven by the higher frequency channels. Retrievals performed without the 85-GHz channels show that using resampled data still results in lower retrieved LWP than the native resolution data due to BFEs, although the differences are about 10% smaller than retrievals with the 85-GHz channels.

The results from this study suggest that an understanding of the issues that arise from data resampling is absolutely imperative when it comes to evaluating parameters retrieved from microwave datasets. As it is intended, deconvolution algorithms allow the same scene to be sampled from each of the microwave channels, however, because of the beam-filling effects due to sub-FOV inhomogeneities in many of the properties that are often retrieved, such as cloud water and rainfall, the resultant retrieved quantity is strongly influenced by whether or not the retrieval algorithm developer has chosen to

resample the input data. Since clouds and rain are not uniform in nature, deconvolution of the high frequency microwave channels to a lower resolution increases BFEs and tends towards reducing cloud emission signatures and retrieved cloud LWP.

The results from this work also show that the common technique of averaging inhomogeneous retrieved parameters from different resolution datasets to a common lower resolution may reduce some of the spatial resolution effects, but they cannot fully account for the beam-filling effects. This stems from the nonlinearities in the relationship between microwave brightness temperature and LWP and has significant implications for climate studies using these datasets. This paper serves as a reminder that choices made on input data resolution strongly influence retrieval results and that intercomparison of averaged retrieved properties that are not homogeneous does not eliminate for beam-filling errors. For users of passive microwave cloud and precipitation datasets, the work in this study shows the effects that data resampling and beam-filling effects may have on retrieval products. It also emphasizes the importance of understanding these effects before undertaking any study utilizing the plethora of available microwave cloud and precipitation retrieval products.

Chapter 3

A Combined Multi-Sensor Optimal Estimation

Retrieval Algorithm for Oceanic Warm Rain Clouds

3.1 Introduction

In an effort to better understand the response of the hydrologic cycle to climate feedbacks, many recent studies have examined the response of tropical cloud processes to changes in SST. The majority of these studies (e.g., Ramanathan and Collins 1991; Lindzen et al., 2001; Hartmann and Larson, 2002) focused on deep convective clouds because of their contribution to total tropical rainfall and the large radiative impacts from the detrained anvil cirrus. However, in the midst of the controversy surrounding many of the theories regarding the response of deep convection to climate change, several studies have suggested another cloud type in the Tropics that may be sensitive to and important for our understanding of the response of the hydrologic cycle to anthropogenic warming. Petty (1999) found warm-topped clouds to be important to the population of precipitating clouds in the Tropics and suggested that the prevailing satellite retrieval methods, namely infrared and scattering-based passive microwave, might be inadequate to resolve these clouds. At the same time, Johnson et al. (1999) drew attention to the importance of

cumulus congestus clouds and suggested a new conceptual model of the tropical hydrologic cycle including this third mode of mid-level clouds, moving away from the more typical model of a bimodal cloud distribution of deep cumulonimbus and trade wind cumulus. And more recently in the Fourth IPCC Assessment, variability in global climate model (GCM) cloud feedback effects was mostly attributed to differences in the models' shortwave cloud feedback, which are dominated by the low and mid-level clouds.

In an analysis using TRMM (Simpson et al., 1996) data, Lau and Wu (2003) further examined the role of warm precipitating clouds in the Tropics. This study exploited the fact that no SST can be retrieved from the TMI when a grid box is completely filled with rain, as would be the case in deep convection, but because of the nature of warm rain clouds, they do not typically fill a grid box and a valid TMI SST can be retrieved. A valid SST in the presence of rain was classified as warm rain and their results suggest that warm rain clouds are responsible for about 31% of the total rainfall in the Tropics. An earlier study by Johnson et al. (1999) indicated that mid-level *congestus* clouds contribute greater than 25% of the total tropical convective rainfall. In light of the fact that *congestus* clouds include both warm rain clouds, as well as those that reach the freezing level and glaciate, the Lau and Wu (2003) estimate is slightly higher than these earlier findings. It is also within the range of estimates by Petty (1999), who combined infrared satellite data with surface and ship stations and found that warm rain clouds were associated with 20-40% of the precipitation reports at these stations. The most recent estimates from CloudSat (Stephens et al., 2002), show that in the west Pacific low and middle clouds make up about 50% of the population of precipitating clouds and over the

entire Tropics, rain falls as frequently from low clouds as it does from both middle and deep convective clouds combined (Haynes, 2008). Each of the previous studies used different definitions of warm rain clouds, which may be responsible for the spread in warm rain estimates. In this study, we define warm rain clouds as clouds that are precipitating and have tops below the freezing level as indicated by infrared brightness temperatures above 273 K.

The 2003 study by Lau and Wu also went a step further to investigate the precipitation efficiency of warm rain clouds. Using a climate model parameterization along with TMI-retrieved cloud liquid water and precipitation, they showed that an increased rate of conversion of cloud water to precipitation with increased SST occurs in warm rain clouds, especially for low rain rates. Their findings suggest that precipitation efficiency of warm rain clouds increases around 8% per degree increase in SST and that this increase in precipitation efficiency in warm rain may be at the expense of cloud water. In a previous study examining the influence of SST on deep convective cloud area, Rapp et al. (2005) used the ratio of cloud area, as defined by TRMM Visible Infrared Scanner (VIRS) infrared brightness temperatures, to rainfall rate from the Precipitation Radar (PR) as a proxy for the precipitation efficiency of rain clouds in the tropical western Pacific. The ratio of deep convective cloud area to rainfall was found to be insensitive to SST, however, warm rain clouds showed an approximate 5% decrease in the ratio of cloud area to rainfall per degree rise in SST. This is similar to the findings by Lau and Wu (2003) and provides more observational evidence supporting their suggestion that the increase in precipitation efficiency may be at the expense of cloud water.

While the findings of these studies are suggestive, each is subject to criticisms. The SST screening method of Lau and Wu (2003) is an ambiguous way of identifying warm rain systems. The study by Rapp et al. (2005) was designed for the identification of deep convection and was not originally intended to examine warm rain systems. The definitions by which the clouds were defined, namely that the clouds must have a rainfall rate greater than 10 mm hr^{-1} , limit the population of warm rain systems observed in that study. With these criticisms in mind, we set out to further investigate the properties of warm rain clouds in the Tropics, but found that available cloud microphysical property datasets disagreed. Both microwave and optical retrievals are readily available to examine the properties of clouds in the Tropics, however, comparison of these products show discrepancies when the clouds are raining. Moderate Resolution Imaging Spectroradiometer (MODIS) 5 km cloud liquid water path (LWP) retrievals (Platnick et al., 2003; King et al., 1997) from the Version 5 Atmosphere Level 2 Joint Product from the Aqua satellite were matched to 0.25° Advanced Microwave Scanning Radiometer (AMSR-E) Version 5 retrievals from Remote Sensing Systems (RSS; Wentz and Meissner 2000) and compared for the tropical western Pacific. While the 0.25° resolution of the AMSR-E retrieval is coarse, each of the microwave channels used in the retrieval has a different FOV, so comparing at finer scales would be questionable. Using the MODIS cloud phase and cloud top temperature along with the AMSR-E rainfall retrieval as a rain mask, we were able to identify warm rain clouds in the tropical western Pacific. We examine this region because it is where warm rain clouds showed the sensitivity to SST in Rapp et al. (2005). Figures 3.1a and 3.1b from MODIS and AMSR-E, respectively, show the sensitivity of LWP retrievals to SST for non-raining clouds. Non-

raining clouds show similar results for both retrievals, with LWP fairly constant over the observed range of SST. However, when examining the two LWP retrievals for the raining, warm clouds in Figures 3.1c and 3.1d, substantial differences are observed. The MODIS retrieval shows a strong decrease in LWP with increasing SST, while the microwave retrieval remains fairly constant. Although not shown here, examination of the MODIS retrievals of effective radius and cloud optical depth also reveals differences between non-raining and raining clouds. In non-raining clouds the effective radius

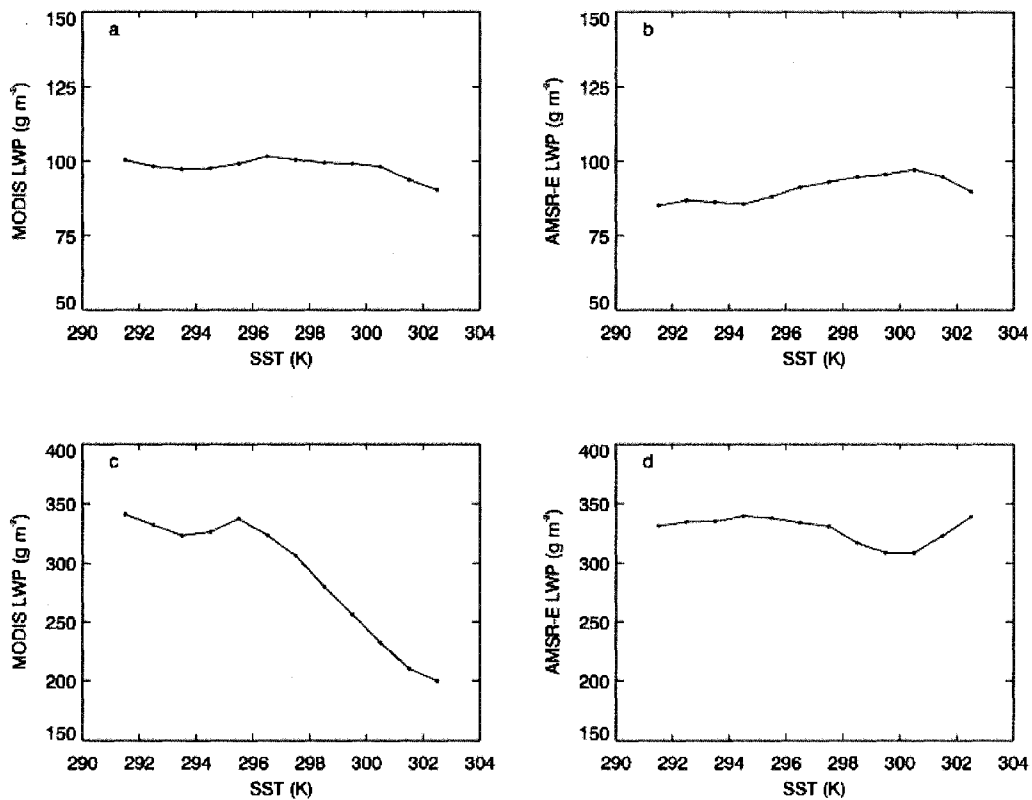


Figure 3.1 Mean LWP (g m⁻²) with SST (K) for non-raining warm clouds for (a) MODIS and (b) AMSR-E and for raining warm clouds for (c) MODIS and (d) AMSR-E.

increases from 12 to 18 μm and the optical depth decreases by about 30%, with the resultant LWP remaining nearly constant with SST. For the warm rain clouds, the effective radius has small variations over the range of SST shown in Figure 3.1, only varying from about 18 to 21 μm . However, the cloud optical depth decreases by about 60% with SST, which is the reason for the large observed decrease in warm rain cloud LWP in Figure 3.1. Results from a modified Nakajima-King retrieval (Nakajima and King, 1990; Nakajima and Nakajima, 1995) applied to the TRMM VIRS data and RSS TMI retrievals show similar behavior.

It is not surprising given the limitations of each of these methods that there are differences, but it illustrates the potential issues with using these retrievals for some climate studies. The microwave retrieval suffers from coarse resolution and may be viewing either clear sky or multiple cloud types within a single footprint containing a warm rain cloud. It is also possible that the coarse resolution affects warm rain cloud identification since these clouds may not fill the entire footprint and the signal may be too weak to retrieve rainfall. This could be why the MODIS cloud optical depth slightly decreases with SST for non-raining clouds since clouds may be misidentified as non-raining. Another issue with the microwave retrieval is that the microwave retrieval is sensitive to both cloud and rain drops, so most retrieval algorithms use a LWP threshold to delineate clouds and rainfall, which can bias the results as shown by Berg et al. (2006) and O'Dell et al. (2008). In the microwave LWP retrieval shown in Figure 3.1, the LWP in raining clouds has a minimum threshold of 180 g m^{-2} and is parameterized as a function of the rain rate and an assumed cloud height based on SST. Because of the

retrieved LWP dependence on the rain rate, the shape of this curve is very similar to the shape of the mean rain rate curve for warm rain clouds.

The visible/near-infrared retrieval calculates LWP as the residual of the retrieval of optical depth from the non-absorbing visible wavelengths and the retrieval of effective radius from the absorbing near-infrared wavelengths. The retrieval of effective radius is only sensitive to the cloud top, so the calculation of LWP could be biased, especially in a raining cloud where the larger drops are more concentrated near the cloud base. It is also possible that in a thick, precipitating cloud, much of the visible radiation may be scattered by the cloud drops before it reaches the rain in the lower portion of the cloud.

Because we are most interested in how the rainfall is affecting the properties of the cloud, rather than the total column properties, we have developed a combined optimal estimation microwave retrieval algorithm that takes advantage of the strengths of these different datasets, as well as uses precipitation information that is available on the TRMM satellite to retrieve a microwave *cloud* LWP in a warm rain cloud. We stress the word *cloud*, because this retrieval estimates the LWP due to only the cloud water in a raining cloud. Using deconvolved TMI brightness temperatures along with cloud fraction information from VIRS and rain water estimates from the Precipitation Radar (PR), this retrieval improves on some of the resolution and sensitivity problems of microwave-only or visible/near-infrared retrievals and it also takes into account the emission and scattering from the rainfall to allow an estimate of LWP associated with the cloud water in a raining cloud.

3.2 Data

The retrieval algorithm developed in this study combines data from microwave, visible/infrared, and precipitation radar sensors in an optimal estimation (OE) retrieval framework. We test the algorithm with data from the TRMM satellite from December 2005 to February 2006 from 30°S-30°N, 130°E-170°W. However, this algorithm could also be applied by combining a visible/infrared sensor with the upcoming Global Precipitation Measurement (GPM) mission sensors. And though more difficult because the CloudSat radar does not scan the entire AMSR-E field of view, it may be possible to apply this algorithm to a combination of AMSR-E, MODIS, and CloudSat.

3.2.1 *Microwave Sensor*

The brightness temperatures used in this retrieval are from the TMI (Kummerow et al., 1998). The TMI is a conically scanning passive microwave radiometer that has eight channels that measure both vertical and horizontal polarizations at frequencies of 10.7, 19.4, 37.0, and 85.5 GHz, and a ninth channel at 21.3 GHz that measures only the vertical polarization. The resolution of the measurements varies with the frequency and ranges from 7 x 5 km at 85.5 GHz up to 63 x 37 km at 10.7 GHz. The resolution difference can be a problem because of the inhomogeneity of the scenes viewed by the different channels. A deconvolution algorithm was applied to resample all of the TMI channels to a common resolution of the 19.4-GHz channel at 30 x 18 km. For the algorithm developed in this study a uniform FOV is a necessity because we are using the VIRS data to calculate cloud fraction within the microwave footprint. This requires that

the microwave data be at a common resolution. The deconvolution algorithm follows the method of Backus and Gilbert (1970) that has been shown to be successful at resolution modification of remotely sensed microwave data in numerous studies (e.g., Stogryn, 1978; Robinson et al., 1992; Farrar and Smith, 1992; Long and Daum, 1998). This method uses a weighted sum of the observed brightness temperatures to construct a set of effective brightness temperatures at a single resolution. The Backus-Gilbert method calculates the weighting coefficients by choosing a factor that minimizes the error in the fit of the solution as well as minimizes the associated noise amplification. Calculating these weighting coefficients is time consuming, but since the TMI antenna patterns and scan geometry are known, the coefficients only need to be calculated once and can then simply be applied to each orbit. While it is possible to resample the data to the resolution of the highest frequency channels, the associated noise becomes very large. Making the enhancement of the 10-GHz channel to the 19.4-GHz FOV increased the noise level from 0.54 K to 1.5 K. Resampling to a higher resolution would result in an even larger increase in noise, above which we felt the accuracy of the retrievals would suffer. As a result, the 19.4-GHz channel resolution was chosen because it was the best combination of enhanced resolution of the low frequency channels with an acceptable level of noise.

3.2.2 Visible/Infrared Sensor

The retrieval we have developed utilizes data from the VIRS on TRMM to characterize the cloud field within a TMI footprint. The VIRS (Kummerow et al., 1998) is a five-channel (0.63, 1.6, 3.7, 10.8, 12.0 μm) scanning radiometer on the TRMM

satellite with a 2.11-km field-of-view at nadir and a swath width of 720 km. For this study, we use the visible and infrared channels as a cloud mask to determine the cloud fraction of a given TMI footprint. The VIRS pixels are collocated and matched to the TMI footprints and the cloud fraction is calculated as the ratio of matching VIRS pixels identified as cloud to the total matching VIRS pixels. A VIRS pixel is considered cloudy if the visible reflectance is greater than that of the characteristic clear-sky reflectance or if the infrared brightness temperature is lower than a threshold determined by the underlying SST. The pixel is further tested for ice contamination by checking that the infrared brightness temperature is not below 270 K and by checking the difference between the infrared channels to identify thin cirrus. The retrieval algorithm developed in this study is only designed for microwave footprints that contain water clouds, so any TMI footprint that contains matched VIRS pixels identified as ice clouds are flagged and no retrieval is performed.

3.2.3 Precipitation Radar

One of the most important additions to this algorithm is the information provided by the TRMM PR. The PR is a 13.8-GHz cross-track scanning phased-array radar with a 4.3-km horizontal resolution at nadir and 215-km FOV. We are using the 2A25 dataset (Iguchi et al., 2000) that contains PR estimates of total precipitable water. This allows us to calculate the emission and scattering of the rainwater. In this way, we can separately calculate the contribution of the rainwater to the forward modeled brightness temperatures and retrieve only the LWP associated with the cloud water. As previously mentioned, almost all other microwave retrieval algorithms typically use a LWP

threshold to distinguish rain, but this method has been shown to result in discrepancies. Using rainwater information from the PR removes the need for thresholding and allows the more realistic treatment of cloud and rainwater necessary for this retrieval.

3.2.4 Ancillary Data

In this study, we specify SST, temperature lapse rate and water vapor scale height for calculating the upwelling radiances in the forward model. The SST data used in this study is retrieved daily from the TMI (Wentz and Meissner, 2000; Wentz et al., 2000) on $0.25^\circ \times 0.25^\circ$ grid. To describe the atmospheric temperature lapse rate and water vapor scale heights, daily values are computed from NCEP/NCAR reanalysis (Kalnay et al., 1996) data on a $2.5^\circ \times 2.5^\circ$ grid. The temperature lapse rate is computed as the average lapse rate from the surface to 250 hPa. To calculate the daily water vapor scale height, reanalysis specific humidity profiles from the surface to 300 hPa are fit with

$$SH = SH_0 e^{-\frac{Z}{H}} \quad (3.1)$$

where SH is the specific humidity at height, Z , SH_0 is the specific humidity at the surface, and H is the water vapor scale height. Uncertainties due to these parameters must be specified in the forward model. For each $2.5^\circ \times 2.5^\circ$ grid box, the standard deviation in lapse rate and scale height is computed for the three month period of study. For the period from January 2005 to February 2005, the region of study in the western Pacific has an average lapse rate of 6.4 K km^{-1} with an average standard deviation of 0.5 K km^{-1} . The average water vapor scale height for this time period and region is 2.6 km with an average standard deviation of 0.6 km. The uncertainties in the forward model brightness

temperatures due to the NCEP/NCAR reanalysis lapse rates and water vapor scale heights are computed from these average standard deviations.

3.3 Retrieval Algorithm

Retrieval of atmospheric properties from microwave measurements is dependent on a number of factors, the forward model, assumptions about the model atmosphere and the uncertainties of the forward model itself, the assumptions in the forward model and in the measurements. In this study we employ the optimal estimation retrieval technique (Rodgers, 1976; Rodgers, 2000; Marks and Rodgers, 1993) for the inversion. An earlier version of our algorithm for non-precipitating clouds is thoroughly described in Elsaesser and Kummerow (2008), however, we have made several modifications to the forward model that allow us to account for partially cloud filled TMI footprints, as well as emission and scattering from rainwater.

3.3.1 Forward Model

Following Elsaesser and Kummerow (2008), the surface reflection and emission are calculated using the Deblonde and English (2001) model, which takes into account non-specular reflection to improve surface emissivity calculations at large viewing angles, and the Kohn (1995) model which improved on Wilheit (1997a,b) model with better treatment of multiple reflections, sea surface roughness parameters, and sea foam. A modified version of the Rosenkranz (1998) model is used to compute gaseous absorption by oxygen, nitrogen, and water vapor. In this study, we are retrieving cloud

systems that may only partially fill the microwave pixels and in which scattering may be present. Because the microwave pixels may contain both clear and cloudy areas, the calculation of brightness temperatures, T_B , in the forward model is formulated as,

$$T_B = (1 - \alpha)T_{BCLR} + \alpha T_{BCLD} \quad (3.2)$$

where α is the cloud fraction as defined by VIRS, T_{BCLR} is the modeled clear sky brightness temperature and T_{BCLD} is the modeled brightness temperature of the cloudy area. It is likely that there are slant path effects that influence our calculation of cloud fraction, however, this is limited somewhat by the fact that we are only using data within the 215 km swath width of the PR. The possible errors associated with the cloud fraction calculation are taken into account within the OE framework and are discussed in the following section. In the absence of rain the Rayleigh approximation is assumed and cloud liquid water absorption calculations are based on the Liebe et al. (1991, 1993) model. When rain is present and the Rayleigh assumption is no longer valid, the calculation of T_{BCLD} includes Mie scattering effects. Using the rainwater estimate and top of the rain column from the PR and assuming a Marshall-Palmer drop size distribution (DSD; Marshall and Palmer, 1948), we calculate the contribution of the rainwater to the upwelling brightness temperature according to Lorenz-Mie theory. These calculations include many assumptions regarding the DSD and the accuracy of the PR rainwater estimates, which must be accounted for within the retrieval. The effects of these assumptions are investigated in more detail in the following section.

3.3.2 Retrieval Approach

Following the work of Rodgers (1976), we employ the optimal estimation approach to the retrieval as in Elsaesser and Kummerow (2008). With the forward model described previously being denoted as F , we can express the TMI satellite measurements, y , as

$$y = F(x, b) + \varepsilon \quad (3.3)$$

where x is the retrieved atmospheric state, b represents other unretrieved a priori parameters in the forward model and ε is an error term containing the uncertainties in the measurements, forward model, and the forward model assumptions. The problem is then to invert this equation by estimation the atmospheric state, x , that most likely produced the TMI measurements, y . Using Bayes theorem, the probability of a x being the true retrieved state given a set of TMI measurements, is proportional to the product of the probability of observing the TMI measurements, y , given a simulated state, x , and the a priori probability that is the atmospheric state,

$$P(x|y) \propto P(y|x) P_a(x). \quad (3.4)$$

The solution of retrieved state, x , occurs when a cost function, Φ , is minimized. The cost function is given by

$$\Phi = (y - F(x, b))^T S_y^{-1} (y - F(x, b)) + (x - x_a)^T S_a^{-1} (x - x_a) \quad (3.5)$$

where S_y represents the uncertainties associated with the measurements and the forward model, S_a represents the uncertainties of the a priori constraints on the retrieved state, and

x_a is the a priori guess at the atmospheric state, x . Using Newtonian iteration, the value for x that minimizes the cost function can be found with

$$x_{i+1} - x_i = S_x [K_i^T S_y^{-1} (y - F(x, b)) - S_a^{-1} (x_i - x_a)] \quad (3.6)$$

where

$$S_x = (S_a^{-1} + K_i^T S_y^{-1} K_i)^{-1} \quad (3.7)$$

is the error covariance matrix of the retrieved parameters and K is the kernel matrix expressing the sensitivity of the forward model to a perturbation in the retrieved parameters. The solution is found by iterating until the difference in retrieved states between successive iterations is less than the number of independent retrieved parameters.

3.3.3 Retrieval Error Diagnostics

One of the benefits of the optimal estimation approach to inversion is that it provides several diagnostics that indicate the quality of the retrieval. In Eq. (3.7), the error covariance of the retrieved parameters provides an estimate of the uncertainty in the retrieved state due to uncertainties in the measurements, the forward model, and in the a priori parameters. Diagonal elements of Eq. (3.7) represent the errors associated with each retrieved variable and the off-diagonal elements represent the correlations between errors the retrieved variables. From Eq. (3.7), it is obvious that the error of the retrieved parameters is dependent on both the uncertainties in the a priori parameters and the

x_a is the a priori guess at the atmospheric state, x . Using Newtonian iteration, the value for x that minimizes the cost function can be found with

$$x_{i+1} - x_i = S_x [K_i^T S_y^{-1} (y - F(x, b)) - S_a^{-1} (x_i + x_a)] \quad (3.6)$$

where

$$S_x = (S_a^{-1} + K_i^T S_y^{-1} K_i)^{-1} \quad (3.7)$$

is the error covariance matrix of the retrieved parameters and K is the kernel matrix expressing the sensitivity of the forward model to a perturbation in the retrieved parameters. The solution is found by iterating until the difference in retrieved states between successive iterations is less than the number of independent retrieved parameters.

3.3.3 Retrieval Error Diagnostics

One of the benefits of the optimal estimation approach to inversion is that it provides several diagnostics that indicate the quality of the retrieval. In Eq. (3.7), the error covariance of the retrieved parameters provides an estimate of the uncertainty in the retrieved state due to uncertainties in the measurements, the forward model, and in the a priori parameters. Diagonal elements of Eq. (3.7) represent the errors associated with each retrieved variable and the off-diagonal elements represent the correlations between errors the retrieved variables. From Eq. (3.7), it is obvious that the error of the retrieved parameters is dependent on both the uncertainties in the a priori parameters and the

uncertainties in the measurements and the forward model. TMI measurement uncertainties are described in Kummerow et al. (1998) and a thorough description of the a priori and forward model parameter uncertainties for non-raining scenes is given in Elsaesser and Kummerow (2008). Table 3.1 gives the uncertainties from Elsaesser and Kummerow (2008) for the SST and cloud height and the values for the uncertainty in lapse rate and scale height have been recomputed from the daily NCEP/NCAR reanalysis values described previously in section 3.2. However, the microwave T_B deconvolution, the addition of fractional cloudiness from the VIRS, and the PR rain characteristics introduces other error sources that must be accounted for.

The contribution to the forward model and measurement error covariance matrix, S_y , due to the resampling of the microwave T_{BS} to a common resolution is computed at each channel and given as σ_{BG} in Table 3.2. It should be noted that the value given in Table 3.2 for σ_{BG} is only for the pixel in the middle of the scan, since it varies with scan position.

Utilizing cloud fraction from the VIRS also introduces uncertainty in the forward model calculations. Errors in the cloud mask due to thresholding techniques and slant path effects influence the weighting of the computed clear and cloudy T_{BS} . Since

Table 3.1 Forward model error sources (in K) for each TMI channel due to assumptions in SST (σ_{SST}), water vapor scale height (σ_{SCLHT}), temperature lapse rate (σ_{LR}), and cloud height (σ_{CLDHT}).

	10V	10H	19V	19H	21V	37V	37H	85V	85H
σ_{SST}	0.35	0.14	0.21	0.07	0.30	0.02	0.18	0.24	0.04
σ_{SCLHT}	0.23	0.28	1.01	1.53	0.45	1.16	1.94	1.85	3.23
σ_{LR}	0.01	0.04	0.09	0.04	0.37	0.05	0.12	0.42	0.23
σ_{CLDHT}	0.04	0.07	0.09	0.18	0.08	0.19	0.42	0.17	0.07

Table 3.2 Forward model error sources (in K) for each TMI channel due to brightness temperature deconvolution (σ_{BG}), assumed cloud fraction errors (σ_{FCLD}), errors in PR rainwater estimates and assumed DSD (σ_{RW}).

	10V	10H	19V	19H	21V	37V	37H	85V	85H
σ_{BG}	1.39	1.35	0.50	0.47	0.43	0.12	0.10	0.09	0.17
σ_{FCLD}	0.12	0.19	0.30	0.50	0.28	0.87	1.57	1.61	3.57
σ_{RW}	0.82	1.38	1.86	3.39	1.59	2.49	5.72	0.93	2.06

developing a better cloud mask is not the goal of this study and there is little information on the uncertainty in the cloud mask, here we use a simple cloud masking technique and assume up to a 30% error in our estimates of cloud fraction. Perturbing cloud fraction 30%, we simulate the associated T_{BS} and calculate the difference from the unperturbed cloud fraction T_{BS} to estimate the contribution of errors in assumed cloud fraction, σ_{FCLD} , shown with the other sources in Table 3.2.

In retrieving rainy scene parameters, the largest source of error comes from uncertainties in the PR-estimated rainwater used as input in the forward model. To calculate the uncertainty in the rainwater estimates, we have used the PR attenuation-corrected reflectivity along with the PR-derived rainwater for warm rain clouds, shown in Figure 3.2. This figure shows that at any given reflectivity bin, there is a wide range of rainwater values depending on whether a convective or stratiform reflectivity-rainwater relationship is used in the 2A25 PR rainfall algorithm. The two different classifications are evident in Figure 3.2 by the split between clusters of points at higher reflectivities, however, over 90% of the warm rain profiles are below about 30 dBZ where the convective and stratiform curves are close to one another. The lack of certainty in storm classification and the scatter within the classifications suggests a mean uncertainty in PR-

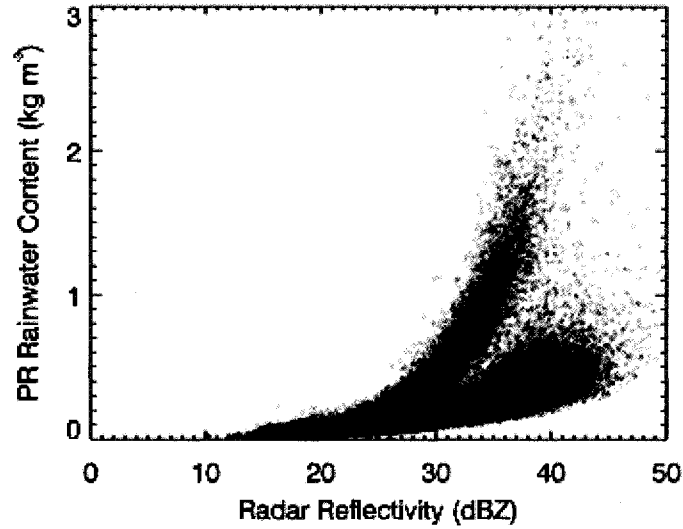


Figure 3.2 PR attenuation-corrected radar reflectivity (dBZ) with rainwater content (kg m^{-3}).

estimated rainwater content of about 50%. This uncertainty in rainwater stems from assumptions made in the PR algorithm regarding the drop size distribution (DSD) of the rainwater. In our forward model, rainwater absorption and scattering are calculated as functions of temperature, DSD, and PR rainwater content. In these calculations we are assuming an exponential DSD

$$N(D) = N_0 e^{-\lambda D} \quad (3.8)$$

with a distribution intercept value, N_0 , of $8 \times 10^6 \text{ m}^{-4}$ as given by the Marshall-Palmer distribution and prescribing the rainwater content and temperature. To maintain consistency between N_0 and the PR rainwater content, we solve for the appropriate slope of the distribution, λ . Because N_0 is prescribed and may not represent the actual

distribution or that assumed by the PR, errors in this assumed value translate into errors in the calculation of absorption and scattering coefficients and ultimately into errors in the simulated T_{BS} .

To test the forward model sensitivity to errors in the rainwater and DSD, the PR rainwater and N_0 values are perturbed by 50% and microwave T_{BS} are simulated. The difference in brightness temperature is calculated from T_{BS} using the original PR estimate and from T_{BS} modeled with the Marshall-Palmer distribution N_0 value. The total error due to PR rainwater and DSD assumptions is given as the sum of the square of the errors. This gives a reasonable estimate of the sensitivity of the forward model T_B computation to PR-rainwater uncertainty and DSD assumptions and is shown as σ_{RW} in Table 3.2.

One useful diagnostic that results from the optimal estimation technique used in this study to evaluate the quality of the retrieval is the χ^2 test where,

$$\chi^2 = (y - F(x, b))^T S_y^{-1} (y - F(x, b)) + (x_a - x)^T S_a^{-1} (x - x_a). \quad (3.9)$$

Generally speaking, χ^2 indicates how well the forward model T_{BS} fit the observations. This should approximately follow a χ^2 distribution with the number of degrees of freedom equal to the number of dimensions of the observations, y , if the forward modeled T_{BS} agree with the observations within the error range. If χ^2 is too small, then measurement errors may have been overestimated or the a priori is too loosely constrained. If χ^2 is very large, then either the forward model inadequately represents the physics or the assumed errors and Gaussian error distribution do not correctly describe the uncertainties in the measurements and the forward model.

3.4 Results

To better understand the results from this retrieval algorithm, it is important to recognize the sensitivity of the retrieval to the addition of the parameters described in this paper. Results after the addition of the VIRS cloud fraction and PR rainwater are compared to the optimal estimation retrieval without this additional information to test the sensitivities. While Elsaesser and Kummerow (2008) validated the non-raining retrieval against both optical and other microwave retrievals, it is nearly impossible to validate LWP retrievals in the presence of rain, especially since we are only retrieving the cloud LWP, not the total. However, we will compare the results of our warm rain retrieval algorithm to the microwave and optical retrievals from Figure 3.1.

3.4.1 Sensitivity to Cloud Fraction

We test the retrieval's sensitivity to cloud fraction by examining the differences in the OE retrieval with and without the VIRS cloud fraction information for the same three months of data in the tropical western Pacific. Figures 3.3a-d show the differences between the retrieved cloud properties (retrieval with cloud fraction minus retrieval without cloud fraction) along with the standard deviation for a given prescribed cloud fraction. Not surprisingly, utilizing the VIRS cloud fraction tends to increase the retrieved cloud LWP especially at very low cloud fractions, however, there is little sensitivity in the TPW and wind speed except at cloud fractions below 20%. This lack of sensitivity to cloud fraction is most likely due to the more uniform nature of the TPW and wind fields compared to the more variable LWP field. From mid- to high- cloud

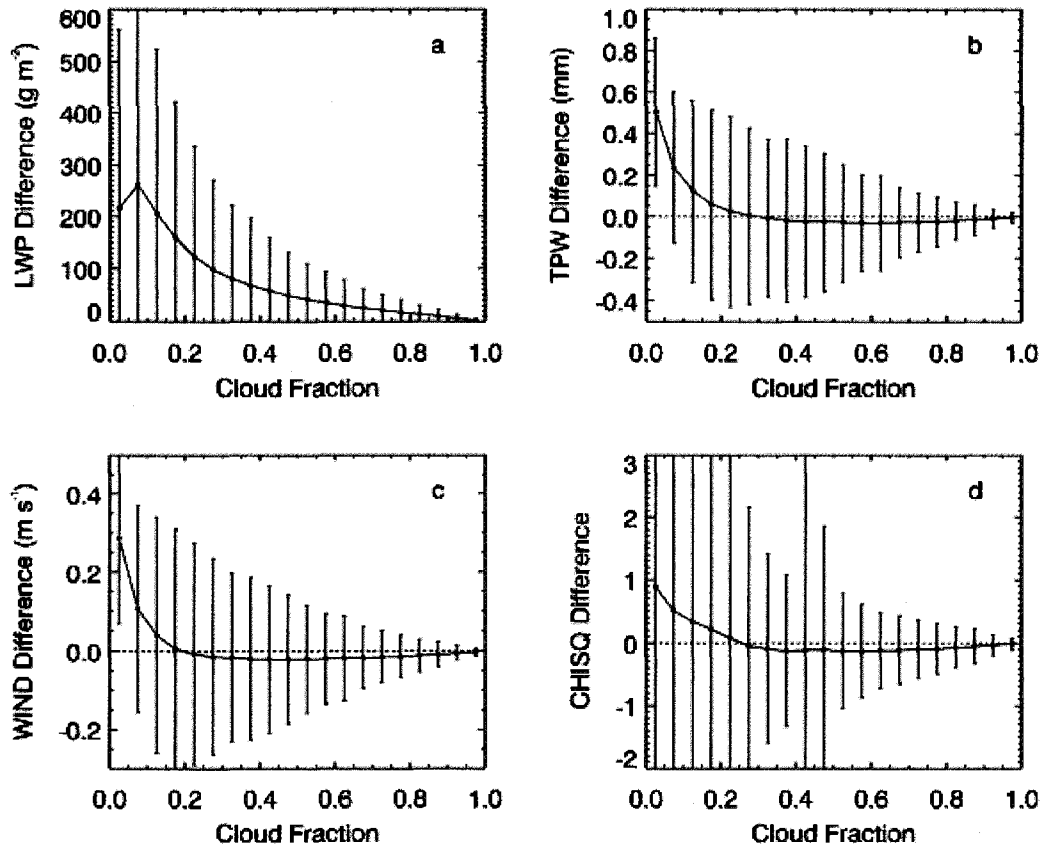


Figure 3.3 Difference in parameters, (a) LWP (g m^{-2}), (b) TPW (mm), (c) wind speed (m s^{-1}), and (d) χ^2 , retrieved with and without cloud fraction plotted against VIRS cloud fraction.

fractions, the use of the VIRS cloud fraction information improves the fit of the retrieved properties, as shown by slightly lower χ^2 values in Fig. 3.3d, but at low- to mid-range cloud fractions, where even the TPW and wind field differences and standard deviations increase due to inclusion of cloud fraction, the resulting retrieved solution tends to be a poorer fit than without cloud fraction. Such low cloud fractions typically do not occur for TMI pixels containing rain, so it will not affect the warm rain cloud retrievals we are most interested in.

3.4.2 Sensitivity to Rainwater

One of the most important additions to this OE retrieval is the inclusion of the PR rainwater estimates, so that the *cloud* LWP can be retrieved in warm rain scenes. By modeling the contribution of the rainwater on the microwave T_{BS} , we retrieve the LWP associated with the cloud and examine the role that precipitation plays in the properties of clouds. Figures 3.4a-d shows the retrieved properties and their standard deviations for warm raining scenes for an OE retrieval with and without the PR rainwater estimates. The inclusion of the rainwater inherently lowers the cloud LWP, but only affects the TPW at the high amounts of column water. At low wind speeds, the inclusion of rainwater increases the retrieved wind speed, while the opposite occurs for the higher wind speeds. While not shown, the majority of the large differences in TPW and wind speeds occurred at the highest rain rates, with the LWP differences being fairly constant for high rain rates. The lower χ^2 values indicate that the retrieved solution is a substantially better fit with the inclusion of the PR rainwater estimates. However, not reflected in these figures are pixels for which the retrieval cannot converge to a solution

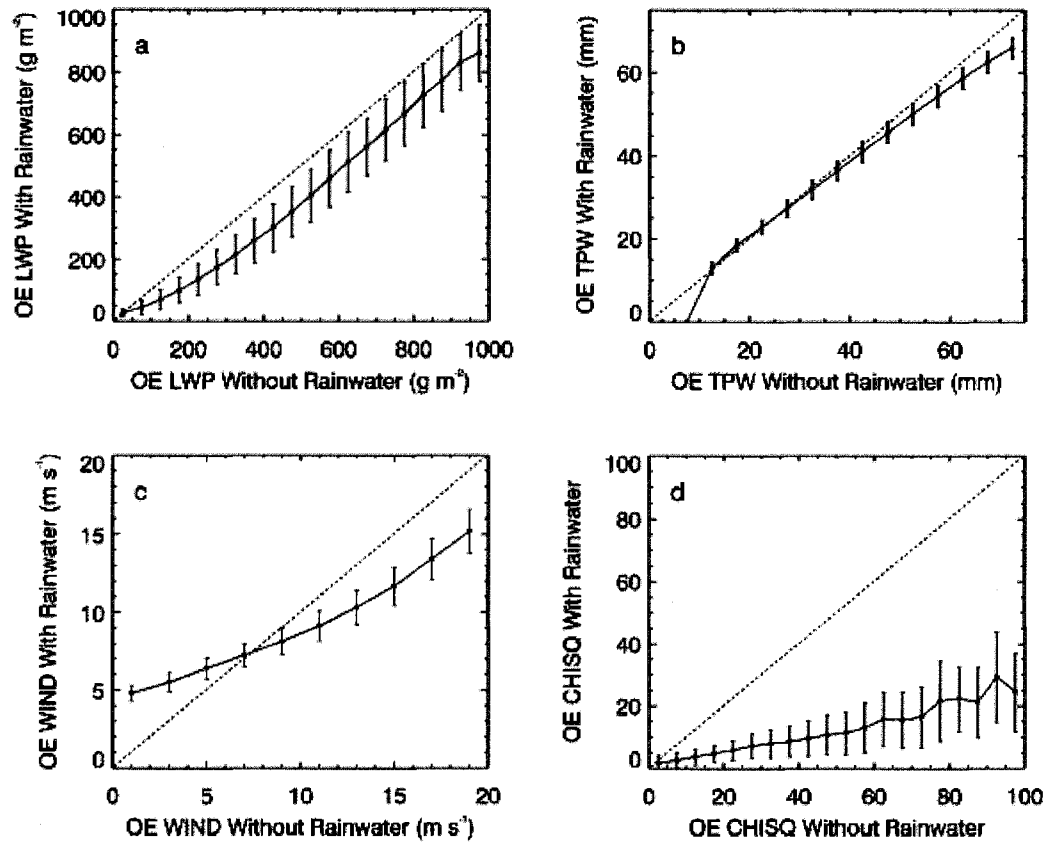


Figure 3.4 TMI OE-retrieved parameters (a) LWP (g m^{-2}), (b) TPW (mm), (c) wind speed (m s^{-1}), and (d) χ^2 , with and without PR rainwater estimates.

with the inclusion of the PR rainwater. Although not frequent, it typically occurs at heaviest rain rates. Figures 3.5a-b depict portion of a TRMM swath that contains many warm rain clouds, as shown by the cloud top temperatures in the VIRS IR T_{BS} and the PR rain rate map. Figures 3.5c-d show the resultant OE LWP retrieval without and with the PR rainwater information, respectively. In Figure 3.5c, the rainfall is evident in the high retrieved LWP, which corresponds to areas of rain in Figure 3.5b. By taking into account the rainwater, the retrieved LWP in Figure 3.5d represents the water in the cloud, not the total water in the column and is much more uniform, as expected in a cloud LWP field. The black areas of the retrieval within the clouds in Figure 3.5d are not pixels with zero LWP, but those in which the retrieval could not converge to a solution. As previously mentioned, they correspond with higher rain rate PR pixels, which most likely indicates that PR rainwater estimate is too high or that our assumptions regarding the rain DSD are inappropriate for this situation.

3.4.3 *Warm Rain Cloud Results*

The results in this section represent a total of over 300,000 TMI pixels containing warm rain clouds with no ice contamination during December 2005 to February 2006 from 30°S – 30°N, 130°W – 170°E. Of the pixels with no ice contamination, precipitating clouds represent 10% of the total population of warm clouds. These results also show that 20% of the total rainfall is due to warm rain clouds. Both of these estimates are probably biased slightly low due to our strict definition of warm rain clouds, as well as the fact that we are excluding TMI pixels that may contain ice. Over

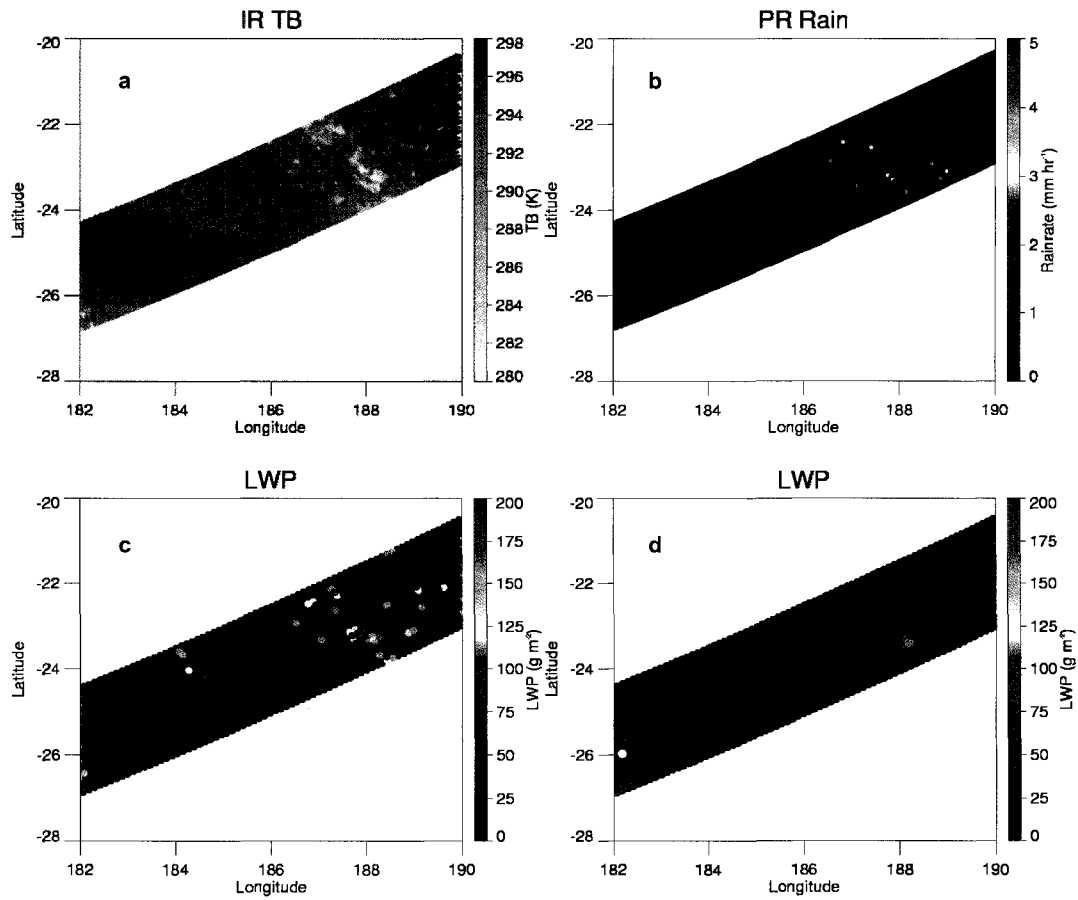


Figure 3.5 Portion of TRMM swath containing warm rain clouds with the VIRS infrared T_B (K) in (a), PR rain rate (mm hr^{-1}) in (b), optimal estimation LWP (g m^{-2}) without PR rainwater estimation in (c), and optimal estimation LWP (g m^{-2}) using PR rainwater estimate in (d).

the range of SSTs observed in this region ($\sim 290 - 304$ K), nearly 75% of the warm rain clouds occurred in a 4 K range of SST from 298 – 302 K. The results from this retrieval are very different for warm rain clouds compared to the AMSR-E microwave retrieval in Figure 3.1. This is expected since the AMSR-E retrieval is more indicative of the total LWP and includes the contribution from the rainwater. Figure 3.6a,b shows the non-raining and warm rain cloud LWP retrievals, respectively, plotted against the underlying SST. Similar to Fig. 3.1, the non-raining cloud LWP in Fig. 3.6a shows very little sensitivity to SST, except for a small spike around 293 K. The non-raining OE retrieval does show a slightly lower mean LWP, around 75 g m^{-2} , with SST than either the RSS AMSR-E ($\sim 100 \text{ g m}^{-2}$) or the MODIS retrieval ($\sim 90 \text{ g m}^{-2}$). Without additional information, it is not possible to assess which retrieval might be more accurate. We can nonetheless conclude that, irrespective of the method, the trends show mean LWP of non-raining clouds is fairly insensitive to SST.

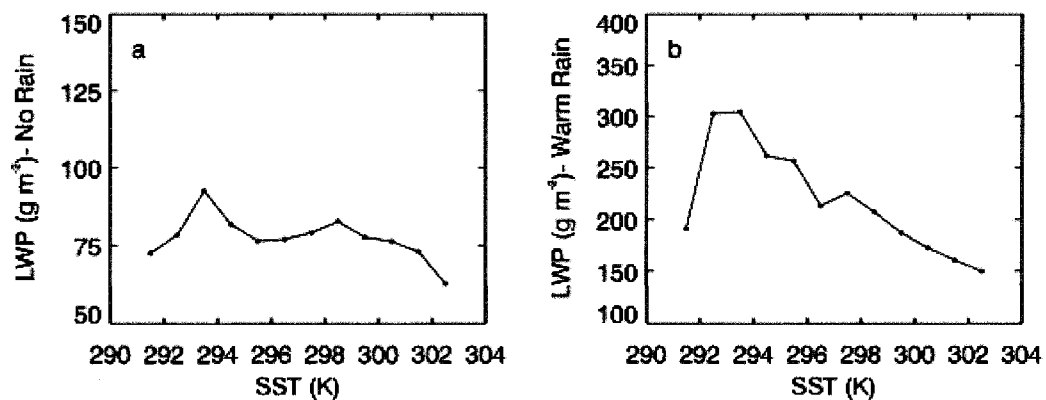


Figure 3.6 Mean TMI OE-retrieved LWP (g m^{-2}) with SST (K) for (a) non-raining warm clouds and for (b) raining warm clouds.

Interestingly, the warm rain OE retrieval in Figure 3.6b shows a very strong decrease in *cloud* LWP with increasing SST. This is in good agreement with the MODIS warm rain LWP results in Figure 3.1. In a thick cloud that contains rain, it is quite likely the majority of the visible radiation has been scattered by the time it reaches the top of the rain column, so the MODIS retrieval is therefore mostly sensitive to the water in the cloud, not in the rain. This may be why the two retrievals operating on entirely different principles, the visible/infrared, which inadvertently does not see the rain, and the microwave OE retrieval, which directly accounts for the rain, yield comparable results. While these results are suggestive and indicate that cloud water may be more efficiently converted to rainfall at higher SST, we can examine the relationship between the rainfall and the cloud properties from our retrievals and determine how their interaction may be affected by surface temperature. Since the warm rain cloud LWP is decreasing with SST in Figure 3.6b, which is counter-intuitive, it suggests that in an increased SST environment, the convection may become more vigorous and the conversion of the cloud water to precipitation may be enhanced, resulting in the scavenging of cloud water for the production of more rainfall. To test this, the ratio of the cloud LWP to PR rainwater is compared in Figure 3.7 to gain a better understanding of how rainfall may be affecting the cloud with changing SST.

The ratio of cloud LWP to PR rainwater in Figure 3.7 also shows a strong decrease with SST. At the lowest SSTs, the ratio of LWP to rainwater is almost two to one, but drops to almost one half at the higher SSTs. There also appears to be a shift in the slope of the decrease in this ratio near 297 K, with the ratio decreasing faster at lower SSTs than higher SSTs. Because we are examining a large region that includes both deep

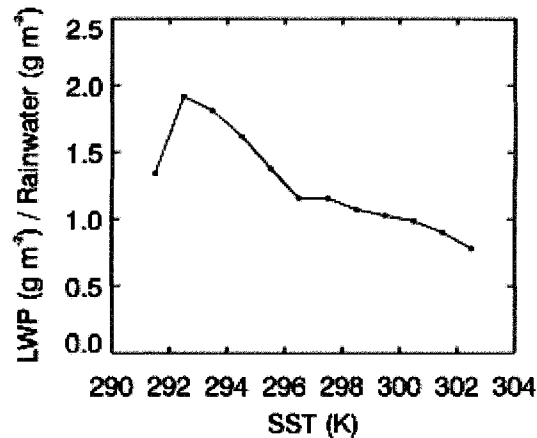


Figure 3.7 Ratio of mean TMI OE-retrieved LWP to PR-estimated rainwater plotted against SST (K).

tropics, as well as subtropical latitudes, this shift may indicate a change in rain regimes not apparent when just examining the relationship of LWP with SST. In the deep tropics, there are very few SSTs that fall below 297 K and examining the locations of the clouds shows that over 99% of the warm rain clouds with SSTs below 297 K occur between 20° – 30° S and 20° – 30° N. Above 297 K, warm rain clouds occur both in the subtropical and tropical regions of our domain. Though not shown here, examining the LWP and rainwater ratio for warm rain clouds only in the subtropical area of the domain shows that the strong decrease of about 10% per degree SST in Figure 3.7 for clouds with SSTs below 297 K, actually extends throughout the full SST range. In the tropical area of our domain, between 20°S and 20°N, where SSTs are above 297 K, the decrease is only about 6% per degree SST. Since clouds in the tropical region of the domain are more numerous, they dominate the trend seen in Figure 3.7 above 297 K. While the dynamics

influencing the clouds in the subtropical and tropical regions of our domain are very different, over the range of SSTs observed in the two different regions, both show that the rainwater is increasing at the expense of water in the cloud.

One issue that has not been addressed is the use of PR rain estimates as the rain/no rain threshold. The PR is only sensitive to rain rates greater than approximately 0.5 mm hr^{-1} , so there is light rainfall from warm clouds that is not being detected. To be sure that this threshold is not biasing the non-raining cloud results, we use a technique suggested by Rosenfeld and Gutman (1994) to identify clouds that may be precipitating below the sensitivity threshold of the TRMM PR. Using the VIRS effective radius retrieved from a modified Nakajima and King scheme, we employ an effective radius threshold of $14 \text{ }\mu\text{m}$ to identify possible raining clouds that may have been included in the previous results and recalculate the mean LWP with SST for the non-raining clouds. Though not shown here, the overall results are not affected by the exclusion of possible precipitating clouds, with both the mean and trends remaining virtually unchanged. While inclusion of these clouds with the warm rain cloud results might be a better representation for all raining clouds, it is impossible with the available data to estimate the amount of rain water in these clouds, which could be anywhere from just above zero up to just below the sensitivity threshold of the PR. However, if the results in Figure 1 of Lau and Wu (2003) are valid, suggesting that the ratio of cloud water to rain rate decreases with SST much more rapidly for low rain rates, then this would only serve to enhance the decreasing trends observed in Figures 3.6 and 3.7.

3.5 Discussion

In order to better understand the interaction between cloud properties and precipitation, an optimal estimation retrieval algorithm was developed for oceanic warm rain clouds that combines information from multiple sensors. By utilizing cloud fraction from the VIRS and rainwater estimates from the PR, we have not only eliminated some of the issues with microwave cloud property retrievals, but also enabled the retrieval of the water associated with the cloud instead of the total LWP. Examining the difference in retrieved parameters due to the addition of VIRS cloud fraction showed very little difference in TPW and wind speed for all but the lowest cloud fractions, with increased LWP for all cloud fractions. Comparing the OE retrieval with and without the PR rainwater estimates showed that the cloud LWP was always reduced in the presence of rain, but the wind speed could be affected in either direction and that the TPW retrieval was lower for higher column water amounts, with both of these differences occurring for the highest rain rates. Evaluation of the results also shows that the added information generally lowered the χ^2 diagnostic, suggesting that the extra information allows for a solution that better fits the measurements.

Examination of the warm rain cloud results shows that the LWP in the cloud, when the rainwater contribution is taken into account, decreases with underlying SST. Both the magnitude and trend in LWP agree well with the MODIS LWP retrieval in the presence of rain, but not the AMSR-E retrieval, since it is sensitive to the total liquid water in the cloud and has the previously mentioned rain/LWP thresholding problem. The ratio of cloud LWP to PR rainwater also decreases with SST. This result is telling because it shows that the increase in rainwater at the expense of the water in the cloud is

enhanced as the surface temperature increases, supporting our conjecture and previous findings. These results suggest that in an increased surface temperature scenario, the rate at which cloud is converted to precipitation will increase, leaving less cloud water to moisten the lower and middle troposphere. Because cloud resolving models typically use an autoconversion threshold that is a function of cloud water content and cloud drop number concentration (e.g., Khairoutdinov and Kogan, 2000), for a given number concentration the availability of more water at higher SSTs will lead to higher cloud water contents and the rate of autoconversion should be increased. Whether or not climate models can reproduce this relationship is questionable. In a follow up to their 2003 study, Lau et al. (2005) examined the sensitivity of a general circulation model (GCM) to microphysical processes that describe the conversion of cloud water to precipitation. They found that increasing the autoconversion rate did indeed lead to more rainfall but less cloud produced by the model. However, this study manually prescribed increases in the autoconversion rates and did not have an interactive autoconversion rate. Del Genio et al. (2005) discussed the deficiencies in many GCM schemes to accurately represent the cloud and precipitation processes and showed that an interactive cumulus scheme can produce results similar to this study for clouds below the freezing level.

The implications of this increase in precipitation at the expense of cloud water have further impacts than just changes to the cloud and radiative properties. In a modeling study, Raymond and Torres (1998) showed that shallow and mid-level convective precipitation efficiency controlled the low and mid-level moistening and found that the moistening provided by these clouds is necessary to precondition the environment for deep convection. Johnson et al. (2001) supported this assertion with

observations from TOGA-COARE that evaporation of cumulus congestus convection in the lower and middle-troposphere preconditions the environment for deep convection. In a study of the mutual regulation of the tropical hydrological cycle and sea surface temperature, Stephens et al. (2004) also presents the humidistat feedback with evidence from TOGA-COARE and TRMM suggesting a ‘destabilization phase’ wherein shallow convection increases and moistens the lower troposphere to condition the atmosphere for deep convection. This moistening of the lower troposphere has also been linked to the timescales for deep convective outbreaks by Bladé and Hartmann (1993), Hu and Randall (1994) and Kemball-Cooke and Weare (2001) and more recently in the previously mentioned Lau et al. (2005) modeling study. The increase in the rate of conversion of cloud water to precipitation as shown by the results in this study, leaves less water available to moisten the atmosphere, which many studies suggest may have implications for the onset of deep convection.

Chapter 4

Interactions Between Warm Rain Clouds and Atmospheric Preconditioning in Tropical Disturbances

4.1 Introduction

Westward propagating synoptic-scale disturbances occur across the Pacific Ocean and the evolution of cloud and precipitation systems linked to westward propagating synoptic scale waves has been the focus of many studies since the 1940's. These easterly waves (Riehl, 1954) or tropical-depression type (TD; Takayabu and Nitta, 1993; Dunkerton and Baldwin, 1995) disturbances occur mostly in northern hemisphere summer on 3-6 day timescales in both the Atlantic and Pacific Oceans with some of them evolving into tropical storms or hurricanes. Recent studies of the structure of TDs (e.g., Peterson et al., 2003; Serra et al., 2008) show that low-level moistening and warming typically occurs ahead of the deep convection associated with the passage of the wave. This moistening and warming begins in the boundary layer several days prior to the deep convection. As the shallow cumulus convection deepens to mid-levels, the moist layer deepens. Using Tropical Ocean Global Atmosphere Coupled Ocean-Atmosphere Response Experiment (TOGA-COARE) data, Johnson et al. (2001) showed that increases in mid-level *congustus* clouds prior to deep convection were associated with the

deepening of the moist layer, which preconditioned the atmosphere for deep convection. This moistening and warming at the lower and mid-levels with upper level cooling and drying serves to increase the convective available potential energy (CAPE) to its peaks just before the passage of a TD trough. This increased instability allows the deep vertical development of convection (Peterson et al. 2003). While it appears that the moistening and warming provides the instability necessary for the deep convection associated with the TD, little attention has been paid to the warm, shallow and mid-level convection connected to these conditions. In a study examining the cloud activity associated with TDs, Cho and Ogura (1974) found that shallow convection was present everywhere in the wave disturbance. Johnson et al. (2001) also showed that the mid-level congestus clouds were present at all times during TOGA-COARE. However, this low- and mid-level moistening appears to only occur prior to deep convection, with the drying and cooling occurring after the deep convection. The fact that shallow and mid-level convection is present throughout a disturbance, but the moistening and warming only occurs ahead of the TD, suggests that a change in the behavior of the convection across the passage of the wave is occurring. The most shallow convection typically does not precipitate and all of the cloud water is available for mixing and evaporation to moisten the lower levels. As convection becomes more vigorous, cloud droplets are able to grow into precipitation-sized particles through collision and coalescence and the cloud produces warm rain. This warm rain depletes some of the water in the cloud and leaves less cloud water available to moisten the low and mid-troposphere through evaporation and mixing. Since mid-level clouds have been shown to be prevalent throughout the Tropics, the deepening of the moist layer only prior to the deep convection suggests that before the TD these clouds

must be more efficient at moistening the lower and mid-troposphere than after the deep convection. Otherwise, the low- and mid-level temperature and humidity fields would not exhibit the structures observed by the aforementioned studies. It should be noted that in this study, we refer to the 'lower' troposphere and boundary layer interchangeably, as the layer below about 850 hPa. We use mid-level to refer to the area above the boundary layer up to the freezing level, from about 850 mb to near 500 hPa. Above 500 hPa is referred to as the upper levels.

As previously mentioned, within the shallow and mid-level convection, there are populations of both precipitating and non-precipitating clouds. The behavior of warm, precipitating convection below the freezing level has been a recent subject of several investigations (e.g., Lau and Wu, 2003; Rapp et al., manuscript submitted 2008). These studies have shown that increases in the precipitation efficiency of warm precipitating clouds strongly influences the cloud amount and cloud liquid water path (LWP), which is related to the amount of water available to moisten the boundary layer and mid-troposphere. While the resultant change in cloud water with precipitation has been hypothesized to control the amount of water available to moisten the lower and mid-troposphere, thus affecting the preconditioning period required for deep convection (Lau and Wu, 2003; Lau et al., 2005; Rapp et al., manuscript submitted 2008), modeling studies have been performed (e.g., Lau et al., 2005; Del Genio et al., 2005) to examine the link between warm rain precipitation efficiency, low-level moistening and recycling timescales for deep convection related only to the Madden-Julian Oscillation (MJO). Lau et al. (2005) found that by increasing the precipitation autoconversion rate for warm rain in a general circulation model (GCM), less cloud was produced with more low-level

condensational heating, which destabilized the atmosphere and led to stronger, but more intermittent MJO events. Using observations, Benedict and Randall (2007) showed that stronger low-level convective heating and moistening associated with cumulus convection prior to deep convection coupled with the MJO led to stronger MJO events and implied that for weak MJO events, the cumulus convection was less effective at preconditioning the atmosphere. However, properties of these cumulus clouds were not examined and observational studies have yet to establish how changes in the properties of the warm rain clouds affect the moistening of the boundary layer and mid-troposphere. The aforementioned studies all examined the MJO, however, the MJO occurs on timescales of 40-60 days, so fewer events are available for study with satellite observations. Also, unlike other convectively-coupled equatorial waves, such as the MJO, TDs form, intensify, and decay in the eastern, central, and western Pacific making them ideal for investigating the relationship between warm rain cloud properties and moistening prior to deep convection across distinct large-scale dynamical environments.

Recently, an algorithm was developed by Rapp et al. (manuscript submitted 2008) for the retrieval of cloud LWP in warm rain clouds. There are quite a few retrievals of cloud LWP already available, but optical and microwave methods yield very different results for warm raining systems due to their limitations when rainfall is present. To overcome some of the problems inherent in visible only or microwave only retrievals, Rapp et al. (manuscript submitted 2008) developed a multi-sensor optimal estimation retrieval algorithm that combines measurements from optical and passive and active microwave instruments on the TRMM satellite. The algorithm uses cloud fraction information from the visible sensor to overcome scene inhomogeneity issues and also

uses the information from the radar to constrain the amount of water in precipitation-sized particles to retrieve the total water, as well as its rainfall and cloud water components. In this way, the retrieved LWP of the cloud water component combined with the rain water gives an important piece of information on the partitioning between cloud and rainwater and allows the investigation of how precipitation processes affect the cloud properties. Results from the Rapp et al. (manuscript submitted 2008) study supported previous findings that over the range of SSTs in the tropical western Pacific, the amount of LWP due to cloud water, when taking into account the amount of water in the rain, does decrease with temperature due to enhanced precipitation.

The algorithm developed in that work now offers a framework for studying the potential effects that this reduction in cloud water in precipitating clouds may have on low- and mid-level moistening. TDs across the Pacific offer an excellent test bed for the investigation of how changes in warm rain cloud properties may contribute to the moistening and heating that is observed prior to the onset of deep convection associated with a TD. The results from the multi-sensor retrieval algorithm are applied here to examine these relationships.

4.2 Data

This study combines a number of datasets to identify TDs, composite dynamic and thermodynamic fields, and to retrieve cloud properties associated with tropical disturbances. Because TDs are most active in the warm seasons, data from April through September in 1998 to 2002 are analyzed. Since we are interested in examining the

variability of the relationship between cloud properties and lower-tropospheric moistening prior to the TD, we choose three locations spanning the Pacific Ocean for analysis; near Kwajalein at approximately 7.5°N, 167.5°E (KWAJ) in the western Pacific, the central Pacific at 7.5°N, 140.5°W (CPAC), and a location in the Tropical Eastern Pacific Process Study (TEPPS; Yuter and Houze 2000) region at 7.5°N, 124.5°W.

4.2.1 Precipitation Data

Many studies have used outgoing longwave radiation or optical depth to perform analyses to identify TDs, however, Benedict and Randall (2007) showed that spectrally filtered precipitation was successful in identifying MJO events. Because of the strong connection between deep convection and heavy precipitation with the passage of a tropical disturbance, we also employ precipitation as the variable on which our analysis is based. The precipitation dataset used for identification of tropical disturbances is the Global Precipitation Climatology Project (GPCP) 1° x 1° daily merged precipitation dataset (Huffman et al., 2001), which blends several observational datasets to produce daily estimates of precipitation. For the equatorial region of interest in this study, GPCP calculates a threshold-matched precipitation index from infrared brightness temperatures where the relationship between the index and precipitation is guided by monthly, local SSM/I precipitation frequency and GPCP satellite-gauge precipitation estimates.

4.2.2 *Thermodynamic Properties*

European Centre for Medium-Range Weather Forecasting (ECMWF) reanalysis (ERA-40) data are used to describe the thermodynamic atmospheric properties associated with the TDs. In the Pacific, rawinsonde and other data sources are sparse, so reanalysis data provides the best description of the TD environment. Comparison with Integrated Global Radiosonde Archive (IGRA; Durre et al., 2006) at KWAJ for the warm season in 2002 shows very good agreement between the ERA-40 temperature and humidity profiles. Temperature differences are less than 1% and differences in specific humidity have a maximum of 8%. The 8% specific humidity differences are mostly confined to the levels near the surface and the differences above the near-surface level are less than about 4%.

The ERA-40 at $2.5^{\circ} \times 2.5^{\circ}$ resolution are used at the three locations over the western, central, and eastern Pacific to produce composites of temperature, specific humidity and vertical velocity profiles coupled with the TD passage. The ERA-40 data are also used to calculate the convective available potential energy (CAPE). The composited fields are given as departures from the background state, which is defined by the mean of the respective fields for the three days prior and the three days after the dates identified as TDs by the procedures discussed in section 4.3. The date identified as a TD is excluded from the calculation of background state because the anomalous values associated with the wave passage are not representative of the background state.

4.2.3 *Precipitating Cloud LWP*

There are multiple retrievals of cloud LWP, both optical and passive microwave, available for the study of LWP in non-raining clouds. However, the limitations of these algorithms mean that their estimates of LWP in raining clouds are questionable. Because we are interested in the role that precipitating clouds play in the moistening of the lower troposphere, we use a multi-sensor algorithm developed by Rapp et al. (manuscript submitted 2008) for the retrieval of cloud LWP in oceanic warm rain clouds. This algorithm combines measurements from the TRMM satellite to estimate the liquid water in the cloud, exclusive of the rainwater. In this way, we can identify how changes in the amount of cloud water left after the rainwater precipitates from the cloud may affect lower tropospheric water vapor and heating and thus, the instability. TRMM Microwave Imager (TMI) brightness temperatures are combined with Visible Infrared Scanner (VIRS) cloud fraction and Precipitation Radar (PR) rainwater estimates to retrieve cloud LWP in the presence of rain. The TMI is a nine-channel conically scanning passive microwave radiometer with horizontally and vertically polarized channels ranging from 10.7 to 85.5 GHz. Because each TMI channel has a different spatial resolution, the TMI measurements are matched to a common resolution of the 19-GHz channel FOV following the methods of Backus and Gilbert (1970) so that we can calculate cloud fraction from VIRS to account for some of the sub-TMI footprint inhomogeneities. The VIRS is a spectroradiometer with five channels at center wavelengths of 0.623, 1.610, 3.784, 10.826 and 12.028 μm with a 2.11-km FOV at nadir. The VIRS pixels are collocated with the TMI pixels and visible reflectance and infrared brightness temperature thresholds from VIRS are used to determine how many matching VIRS

pixels within the TMI footprint are cloudy. This cloud fraction is then used in the forward model of the optimal estimation algorithm to weight the simulated TMI brightness temperatures of the cloud. Besides accounting for clear and cloudy areas within the TMI footprint, the algorithm also uses PR rainwater estimates to calculate the emission and scattering of the rain so that the LWP associated with only cloud water can be retrieved.

Passive microwave instruments, like the TMI, are sensitive to the emission from the total column integrated liquid water content. Integrated liquid water contents are proportional to the sum of r^3 , where r represents the droplet radius. The power returned to an active radar by water droplets is dependent on the backscattering cross-section of the particles, which is proportional to the sum of r^6 . This r^6 dependence means that the larger, precipitation-sized drops dominate the radar signal and allow us to estimate the amount of water in the column that is associated with rain drops. We can exploit these sensitivities by combining the total water sensitivity of the TMI with the rainwater estimate of the PR to estimate the residual cloud liquid water that is required to match observed TMI brightness temperatures.

The PR is a 13.8-GHz cross-track scanning phased array radar with an approximate 4.3-km resolution at nadir. PR pixels are matched to the TMI pixels and PR estimates of total precipitable water from the TRMM 2A25 dataset (Iguchi et al., 2000) are used to define the mean rainwater amount used in the retrieval algorithm. The PR rainwater estimate is then used in Lorenz-Mie calculations to calculate the emission and scattering contribution of the rainfall to the simulated brightness temperatures. The optimal estimation algorithm then iterates until the simulated solution for cloud LWP is

found that best matches the TMI measurements. The retrieved cloud LWP is used in this study to examine the relationship between precipitating cloud properties and lower- and mid-tropospheric moistening. It is important to note that we are most interested in the water available for mixing and evaporation to moisten the lower- and mid-troposphere. Therefore, when we are discussing non-precipitating clouds, the LWP refers to the total integrated column water content in the cloud. However, when referring to warm, precipitating clouds, the cloud LWP represents only the retrieved cloud water content available for moistening, not the total or rainwater content.

4.3 TD Identification

Lau and Crane (1995) described a method where they used occurrences of maximum cloud optical depth to identify synoptic disturbances. For each warm season in their analysis, nine key dates of maximum cloud optical depth associated with tropical disturbances were identified. The corresponding dynamic and thermodynamic fields were composited over the entire set of identified key dates. To identify deep convection associated with TDs, we employ the methods of Lau and Crane (1995) to select a set of key dates at each of the three locations, KWAJ, CPAC, and TEPPS, that correspond to heavy precipitation events in the GPCP data for the six-month warm seasons (April-September) over the five years of study. For each warm season, nine dates with the highest precipitation amounts for each location are identified. As in Lau and Crane (1995), the dates are required to be separated from each other by at least four days. When two key dates fail to satisfy this requirement, the date with the lower precipitation amount is replaced with another date that was ranked just below the initial set of nine

dates. Figure 4.1 illustrates the success of this method and depicts two TDs that were identified on the key date of 14 July 2000 at the TEPPS and CPAC locations. The clouds coupled with the TDs exhibit the typical inverted 'V' pattern associated with synoptic-scale waves.

To examine the evolution of tropical disturbances, the ERA-40 temperature and specific humidity and wind anomalies are calculated from three days prior to three days after each identified key date. The anomalies in cloud LWP are also calculated from the optimal estimation retrievals for both raining and non-raining clouds. Each of these fields from individual tropical disturbances are then averaged to obtain the composites for each location.

4.4 Results

4.4.1 KWAJ

The ERA-40 composite profiles of temperature, specific humidity and vertical velocity anomalies for the 45-key maximum precipitation dates identified are shown Figure 4.2a-c. Lag 0 represents the date of maximum precipitation identified as a TD, with negative lags representing the three days prior and positive lags representing the three days after the TD. The temperature profile at KWAJ shows a strong cold anomaly centered near 700 hPa and another one near the surface beginning one day prior to the maximum precipitation and continuing two days after, due to strong downdrafts in deep convection. A warm anomaly aloft also associated with the deep convection is present. The deep convection also transports moisture throughout a very deep layer extending

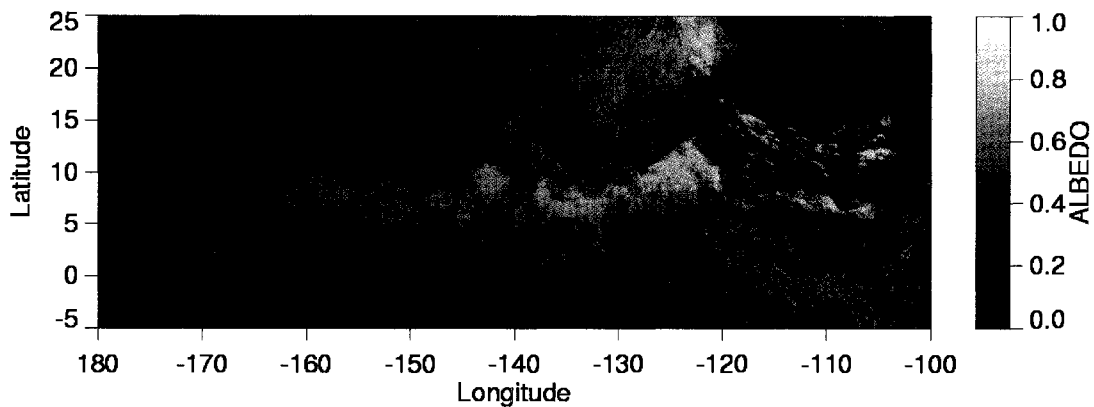


Figure 4.1 GOES-10 visible albedo on 14 July 2000, where TDs are identified at both the TEPPS (T) and CPAC (C) locations.

from the surface up to 250 hPa from Lag -1 to Lag +1, with the mid- to upper-levels remaining moist to Lag +2, presumably from stratiform precipitation. From Lag -3 to Lag -1 there are also positive temperature anomalies at both low and mid-levels. However, the mid-level warming from Lag -3 to Lag -2 occurs with negative specific humidity anomalies associated with subsidence drying as seen by the positive vertical velocity anomalies in Figure 4.2c. From Lag -3 to Lag -2, the low-level warming occurs with moistening and nearly neutral vertical velocity anomalies. At Lag -2 the low-level specific humidity anomalies show a strong positive increase with the strong mid-level positive moisture anomalies increasing slightly later between Lag -2 to Lag -1. Cloud LWP anomalies for raining and non-raining clouds are shown in Figure 4.3a, with the CAPE anomalies shown in Figure 4.3b. Figure 4.3a shows that this low- and mid-level warming with moistening starting about two days prior to the TD is coincident with positive cloud LWP of precipitating cloud anomalies. Although non-raining clouds are present, there is almost no variability in their properties at KWAJ throughout the passage

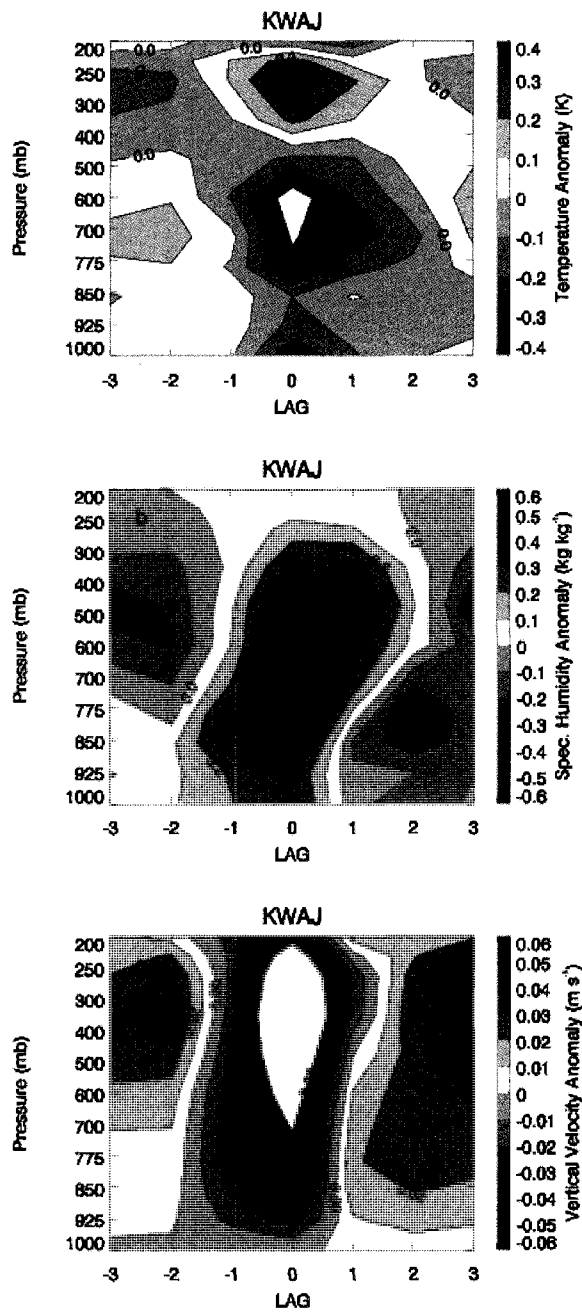


Figure 4.2 ERA-40 anomalies in (a) temperature (K), (b) specific humidity (kg kg⁻¹), and (c) vertical velocity (m s⁻¹) at KWAJ (167.5°E, 7.5°N).

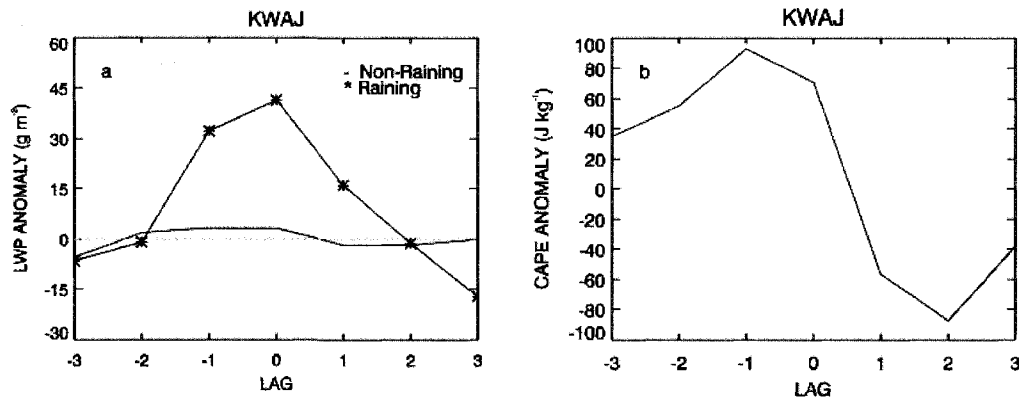


Figure 4.3 (a) Cloud LWP anomaly (g m^{-2}) and (b) CAPE anomaly (J kg^{-1}) composites for TD events at KWAJ (167.5°E , 7.5°N).

of the TD. Anomalies in cloud LWP of precipitating clouds increase up to their max at Lag 0 and begin to decrease after TD. These raining clouds with increasing cloud LWP suggest that the raining clouds are becoming thicker. While this could be occurring simply due to a deepening of the precipitating clouds, examining anomalies in the ratio of cloud LWP to rainwater in Figure 4.4 demonstrates that this ratio increases with the positive LWP anomalies. This implies that the clouds are not as efficient at precipitating before the TD, leaving more of the cloud to mix or evaporate and moisten the lower troposphere. The anomaly in the ratio of cloud water to rainwater peaks at one day prior to the TD and the peak LWP anomaly. Therefore, despite the peak in cloud LWP of precipitating clouds with the TD, clouds are likely most (least) efficient at moistening (precipitating) one day prior to the TD. This agrees well with the strong increase in humidity anomalies of the boundary layer and mid-levels one day prior to the TD. After the TD, the anomalies in the ratio of cloud LWP to precipitation strongly decreases, suggesting less cloud due to more precipitation. Examining the CAPE anomalies in

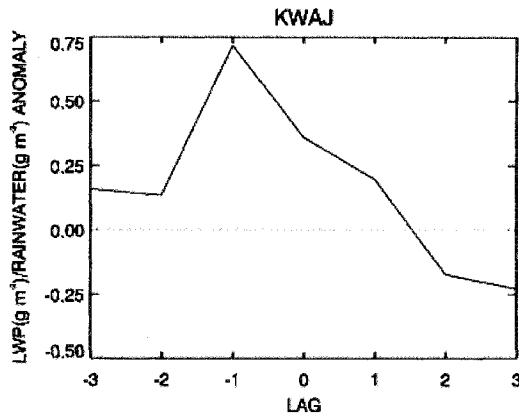


Figure 4.4 Composite of the anomaly in ratio of cloud LWP to rainwater for precipitating clouds for TD events at KWAJ (167.5°E, 7.5°N).

Figure 4.3b shows that the CAPE values are above average throughout the days before the TD and sharply decrease after the deep convection. The shape of the curve of the CAPE values strongly resembles the warm rain cloud LWP curve in Fig. 4.3a because of the moistening and warming related to positive anomalies in cloud LWP of precipitating clouds at the lower levels producing more instability.

4.4.2 CPAC

The evolution of the structure of the thermodynamic and cloud fields at the central Pacific location shows some variations from the KWAJ location. Figures 4.5a-c depict the ERA-40 composites of temperature, specific humidity, and vertical velocity anomalies, respectively. The raining and non-raining cloud LWP anomalies and CAPE anomalies at CPAC are shown in Figures 4.6a-b. In the CPAC region, the temperature, humidity, and vertical velocity anomaly fields show strong subsidence warming and

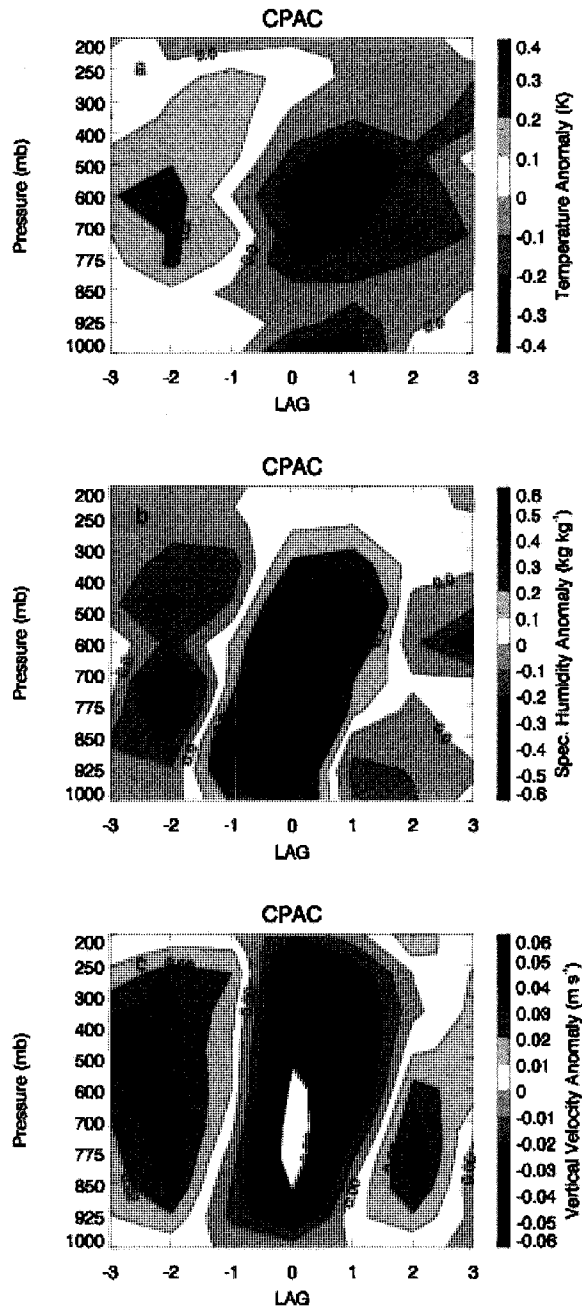


Figure 4.5 ERA-40 anomalies in a) temperature (K), b) specific humidity (kg kg^{-1}), and c) vertical velocity (m s^{-1}) at CPAC (140.5°W , 7.5°N).

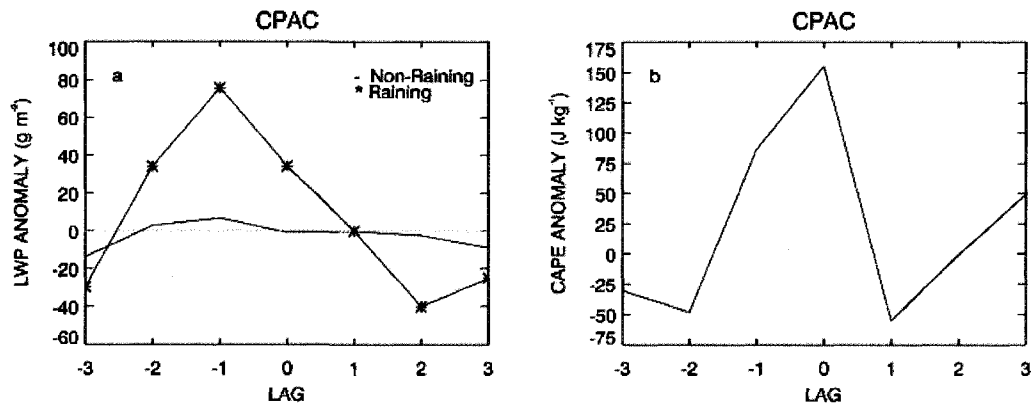


Figure 4.6 (a) Cloud LWP anomaly (g m^{-2}) and (b) CAPE anomaly (J kg^{-1}) composites for TD events at CPAC (140.5°W , 7.5°N).

drying all the way from 850 hPa to 250 hPa at Lag -3 to Lag -2 with little upper-level radiative cooling as seen at KWAJ. About two days prior to the TDs, below 850 hPa positive heating and moistening anomalies begin and by one day prior, the positive anomalies extend up to the mid-levels, indicated by the slight bulge in both the temperature and humidity anomalies. However, compared to KWAJ the deep convection associated with the TD at Lag 0 appears to be less vigorous. The mid- and low-level cooling and drying associated with the deep convective downdrafts and the upper level heating associated with latent heat release are much less at CPAC than at KWAJ. The vertical velocity anomalies are also weaker and peak at much lower levels, 750 hPa, compared to the 300 hPa peak at KWAJ. Despite it being less vigorous than at KWAJ, deep convection associated with the TD continues after the peak in precipitation, as evidenced by the upper-level negative vertical velocity anomalies and mid- to upper-level cooling extending to Lag +2. Again, coincident with positive heating and moistening anomalies, there are positive anomalies in cloud LWP of precipitating clouds beginning

at Lag -2, with almost no change in the properties of non-raining clouds. Unlike KWAJ, the anomalies in cloud LWP of precipitating clouds peak one day prior to the day, not coincident with the TD, however the CAPE anomalies are highest at Lag 0 and strongly decrease thereafter. Also different from KWAJ, at CPAC the CAPE anomalies are not high throughout the three days prior to the TD. It only begins to increase when the anomalies in cloud LWP of precipitating clouds are positive and low-level heating and moistening occur. The lower CAPE anomalies at Lag -3 at CPAC are probably due to the fact that the upper-levels are not as cold and dry as KWAJ prior to the TD.

4.4.3 *TEPPS*

Compared to the other two sites, the TEPPS location, shown in Figures 4.7a-c, exhibits the weakest anomalies in the thermodynamic fields and a different structure, especially in the humidity field. In Figure 4.7a, the temperature structure looks more like that of CPAC than KWAJ, although there is some upper level radiative cooling prior to the TD and stronger upper level heating from deep convection present at TEPPS at Lag 0. Prior to the TD the TEPPS location shows strong subsidence warming and drying from about 800 hPa to 400 hPa, slightly more shallow than at CPAC. There is also strong low-level heating coincident with very strong moistening beginning earlier at TEPPS than the other two locations. This moistening extends from the surface to about 700 hPa from Lag -2 to Lag 0 where there are two maxima in the moisture anomalies, one at 775 hPa and another at about 450 hPa. Positive moisture anomalies after the TD from the mid- to upper levels are more long-lived and deeper than at either KWAJ or CPAC, as evidenced by the upright specific humidity anomaly extending from about 750 to 250 hPa. At

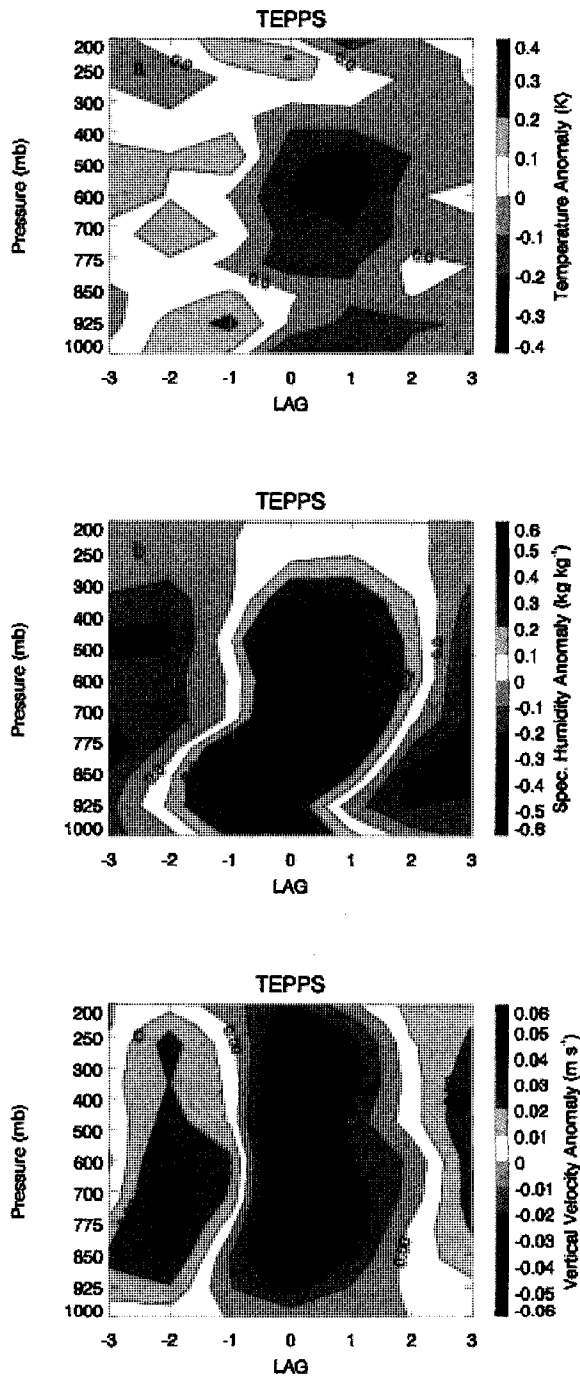


Figure 4.7 ERA-40 anomalies in a) temperature (K), b) specific humidity (kg kg^{-1}), and c) vertical velocity (m s^{-1}) at TEPPS (124.5°E , 7.5°N).

KWAJ and CPAC, the dry layer at low levels begins to deepen between Lag 0 and Lag +1, but at TEPPS the drying from the low to mid levels happens more slowly. This is supported by the vertical velocity anomalies that show upward motion near 750 hPa and 300 hPa extending into two days after the TD, whereas at CPAC and KWAJ upward motion was contained in the upper levels. The cloud LWP and CAPE anomalies in Figure 4.8a-b also show evidence for more long-lived convection after the TD. Large anomalies in cloud LWP of precipitating clouds occur prior to the TD and peak at Lag -1 as at CPAC, however, they do not decrease as quickly and extend to about one and half days after the TD. This supports the lower level upward vertical velocity anomaly after the TD, as well as the positive specific humidity anomalies extending to lower layers for longer than at KWAJ and CPAC. The CAPE anomalies in Figure 4.8b also show that the CAPE begins to increase slightly earlier than at CPAC, likely related to the earlier positive anomalies in cloud LWP of precipitating clouds, heating, and moistening anomalies at low levels. Positive CAPE anomalies reach their max at Lag 0, but they do

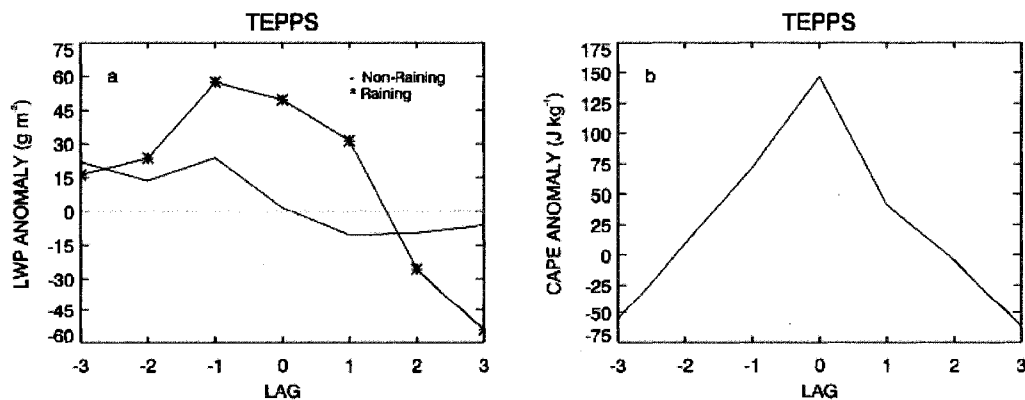


Figure 4.8 (a) Cloud LWP anomaly (g m⁻²) and (b) CAPE anomaly (J kg⁻¹) composites for TD events at TEPPS (124.5°W, 7.5°N).

not fall off immediately as at CPAC and KWAJ. The positive anomalies continue past Lag +1 in support of the other variables that show there is some ongoing convective processes at TEPPS after the maximum in deep convective precipitation.

Another interesting difference at TEPPS compared to the other two locations is the larger positive anomalies in cloud LWP of non-precipitating clouds, which may be contributing to the strong low-level moistening prior to the TD. However these results may need to be viewed with caution. At this location where drizzling clouds are more common, it is possible that this anomaly in the non-raining clouds is due to precipitating clouds that have rain rates that are below the PR's sensitivity threshold of 0.5 mm hr^{-1} . These clouds would not be identified by our algorithm as raining and therefore would be retrieving a larger total LWP that would be solely attributed to cloud.

4.4.4 Influence of SST

Much of the study of the variability in warm rain clouds is based on their response to SST. Studies by Lau and Wu (2003) and Rapp et al. (2005, 2008) showed that as the SST increases, warm rain cloud amount and LWP decreases due to increasing precipitation. These studies point to a fundamental change in the relationship between clouds and precipitation with SST. While there is some change in SST across the passage of a TD, with a peak approximately two days before and a minimum about a day after, this variation is very small ($\sim 0.1 \text{ K}$) because of the short timescales. However, when examining the cloud properties and CAPE values of TDs in different mean SST environments, a pattern emerges. Figures 4.9a-c show the anomalies in cloud LWP of precipitating clouds at each location for TD events separated by the mean SST

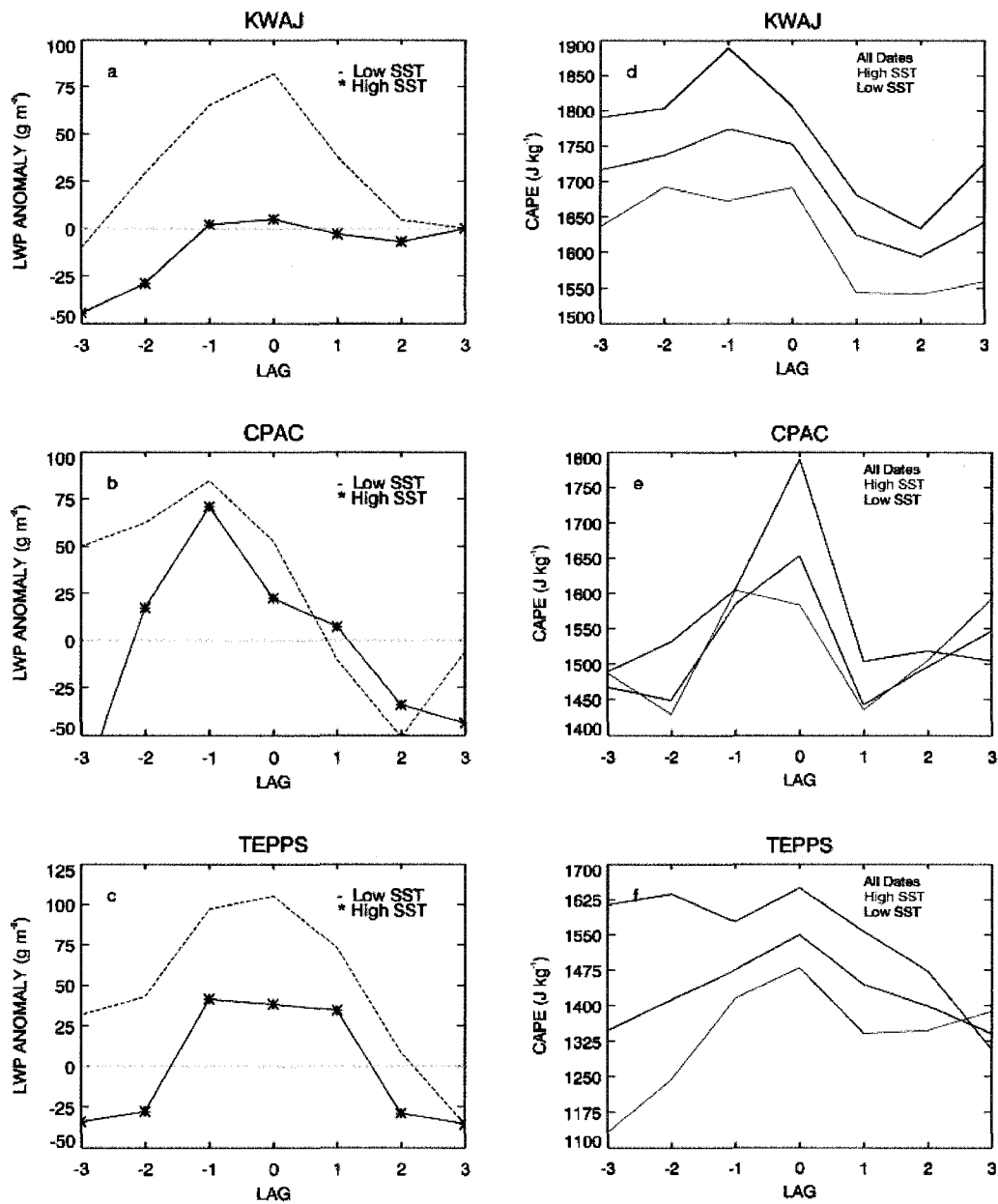


Figure 4.9 Cloud LWP anomalies (g m^{-2}) composited for (a) KWAJ, (b) CPAC, and (c) TEPPS, and CAPE (J kg^{-1}) composites at (d) KWAJ, (e) CPAC, and (f) TEPPS separated by high and low mean SSTs.

environment. The mean SST is calculated for each location over all of the events and for each seven-day period surrounding the TD. The mean of the TD event is compared to the mean for all events and those TD events with a higher mean SST are labeled in Figs. 4.9 as 'High SST' and events with a mean SST lower than the mean for all events are labeled 'Low SST'. Each of the locations exhibited about a 1 K temperature difference between the high and low SST events. The average temperature for the high and low SST events is 301.7 K and 302.6 K, respectively, at KWAJ, 300.3 K and 301.3 K at CPAC, and 300.6 K and 301.5 K at TEPPS. At each location the curves of anomalies in cloud LWP of precipitating clouds are higher for low SST events than for high SST events. While this may seem counterintuitive, the LWP in the cloud, when the rainwater is accounted for, is lower at higher SSTs due to enhanced precipitation processes depleting the cloud water. This is very apparent at KWAJ in Figure 4.9a where there is little anomaly in cloud LWP of precipitating clouds at high SSTs, but very large anomalies in cloud LWP of precipitating clouds at low SST. Figure 4.9d illustrates the CAPE values at KWAJ for the same events, as well as the mean. This shows that for lower SST TD events, there are larger CAPE values than for the higher SST TD events, suggesting more instability in low SST events than high SST events. Although low-level moistening and heating related to anomalous cloud LWP are not the only factors affecting CAPE, they are a very large contributor to instability and most certainly account for some of the increase for low SST events. At the CPAC location, in Figures 4.9b and 4.9e, the differences between the high and low SST events are much smaller than at KWAJ. This is also reflected in the CAPE curves at CPAC being pretty close together except for at Lag 0. Interestingly, the mean SST at CPAC is lower than at either of the other locations, but the variability of 1

K in SST between the low events and high events is comparable to the 0.9 K differences at KWAJ and TEPPS. At TEPPS, similar to KWAJ, there is a large difference between the anomalies in cloud LWP of precipitating clouds for high and low SST TD events. Throughout the seven-day period the anomalies in cloud LWP of precipitating clouds at TEPPS are almost twice as high for low SST TD events as for high SST events. Like at KWAJ, the CAPE values for low SST TDs are higher. The days prior to the TD also show similar behavior to KWAJ where the CAPE values are high throughout this period and then decrease after the TD a bit more slowly than at KWAJ, which corresponds to the higher anomalies in cloud LWP of precipitating clouds for the TEPPS location after the TD.

The higher CAPE values for low SST TD events is a direct result of enhanced moistening and warming of the low and mid levels related to the higher anomalies in cloud LWP of precipitating clouds. Composites of the thermodynamic fields for TD events separated by SST shows less moistening and warming at the low and mid levels prior to the TD when SSTs are high. The positive temperature anomalies are much deeper and stronger (~ 0.3 K) extending from the surface to about 750 hPa by Lag -1 for low SSTs, but only exist in the boundary layer up to about 850 hPa by Lag -1 with peak anomaly of only 0.1 K for high SST TDs. The positive humidity anomalies for low SST TD events are also stronger, start earlier and build gradually for low SST TDs. At Lag -2, very strong moist anomalies already extend throughout the boundary and by Lag -1 the positive moist anomalies have deepened into the mid levels for low SST TDs. For high SST TDs, the moist anomalies are delayed until Lag -1, though they are comparable in magnitude to the anomalies for low SST events.

While increased positive anomalies in cloud LWP of precipitating clouds seem to be related to increased CAPE at lower SSTs, examination of the GPCP rain rates at each location for low and high SST TDs in Figs. 4.10a-c shows that deep convection results in more precipitation, despite the lower CAPE values, at higher SSTs. Other factors clearly play a role in determining the strength and timing of deep convection. Very strong differences in zonal wind components illustrate one reason why differences between low and high SST rain rates are observed. The zonal wind anomalies for low SST events in Figure 4.11a and for high SST events in Figure 4.11b show that strong wind shear is present for low SST TDs that is not present in the high SST events. This strong wind shear provides a likely explanation for why weaker deep convection with lower rain rates, despite the higher CAPE, is observed for lower SST TD events. At CPAC shear is also stronger for low SST TDs, however, at KWAJ zonal wind profiles are more similar between high and low SST events, with only slightly more shear at low SSTs. This is likely why temperature and moisture anomalies appear more vertically aligned with maximum precipitation than at the other locations and why precipitation differences in different SST environments are smaller.

4.5 Summary

Over a period of five warm seasons, TD events were identified using maximum precipitation occurrences in three locations across the Pacific Ocean following the methods of Lau and Crane (1995). Composite TD thermodynamic structure and associated cloud LWP anomalies as a function of the days before and after the maximum precipitation events were constructed. The composited thermodynamic fields revealed

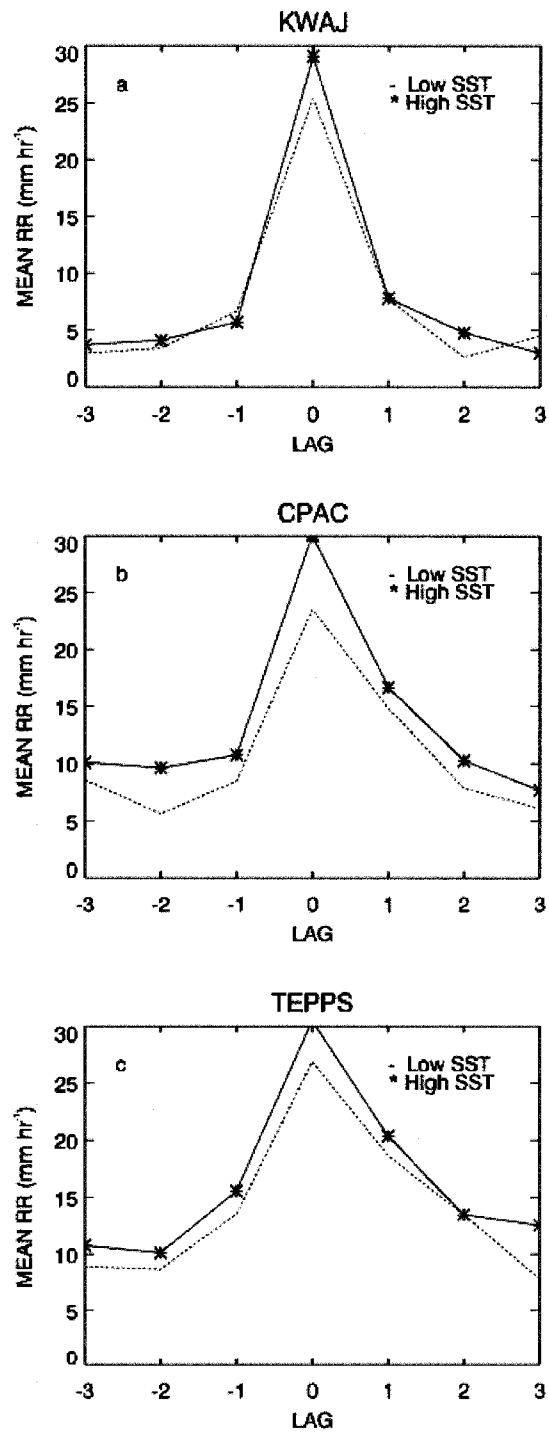


Figure 4.10 Mean rain rate (mm hr⁻¹) composites for high and low SST TD events at (a) KWAJ, (b) CPAC, and (c) TEPPS.

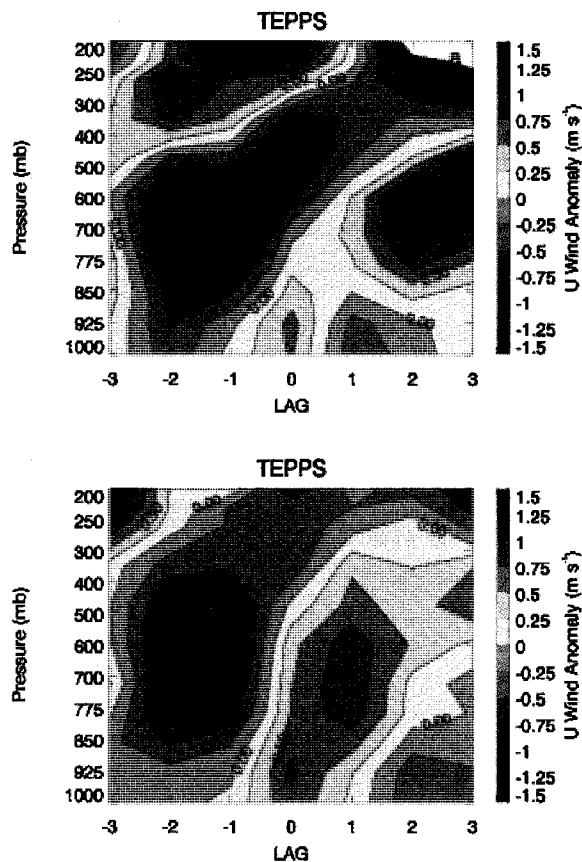


Figure 4.11 Zonal wind anomalies (m s^{-1}) for TD events with (a) low SSTs and (b) high SSTs.

temperature and humidity structures similar to that found by other studies. Ahead of the TD, moistening and warming occurs in the low and mid levels while the upper levels generally exhibit cooling and drying, which leads to an increase in the CAPE. Vertical velocity anomalies ahead of the TD showed subsidence through a very deep layer with rising motions present in the lowest layers beginning about two days prior to the precipitation maximum. Concurrent increases in cloud LWP of precipitating clouds and relatively no change in non-raining cloud LWP suggest that the low-level moistening and warming anomalies are related to the properties of the warm raining clouds. At the time

of maximum precipitation, when CAPE and vertical ascent are strongest a very deep layer is moistened and downdrafts associated with deep convection cool the low and mid levels while condensational heating warms the upper levels, though at some locations more than others. Anomalies in cloud LWP of precipitating clouds begin to decrease at the same time as the precipitation maximum indicating a shift to more efficient precipitation processes in warm clouds. After the TD, the profiles shift to descent with cooling and drying in the low levels with some residual mid- to upper-level ascent and moistening continuing about two days after the TD. CAPE values are rapidly depleted by the deep convection in the days following the precipitation maximum. After the TD, when low levels are dry and cool, the warm rain clouds present have lower cloud LWP anomalies. The thermodynamic structures shown here agree well with the previous eastern Pacific study by Petersen et al. (2003) and Serra and Houze (2002), as well as those shown by Serra et al. (2008) across the Pacific. However, this study highlights the role that warm rain clouds play in preconditioning the atmosphere prior to deep convection associated with TDs.

Previous studies examining the sensitivity of warm rain cloud precipitation efficiency and cloud properties showed that there is a strong relationship with SST. By separating the TD events into those above and below the mean SST for each location, this sensitivity was highlighted. For higher SST events, anomalies in cloud LWP of precipitating clouds were actually lower than those for lower SST events due to the more efficient precipitation process at higher SSTs depleting more of the cloud water. Because less cloud water is available to moisten and destabilize the lower troposphere in high SST TD events, CAPE values were also lower at high SSTs than at low SSTs. However,

GPCP precipitation showed that CAPE is not necessarily a good indicator for the strength of the deep convection with higher rain rates occurring at lower CAPE values in the warmer SST environment. Strong zonal wind shear appears to play a significant role in producing weaker deep convection in low SST environments.

While we have shown that anomalies in cloud LWP of precipitating clouds correspond to heating and moistening prior to deep convection, two major issues remain. First, it is not clear from these results whether the initial heating at low levels occurs due to the convection or another process. It is possible that there is a feedback effect between the initial low-level heating, perhaps due to sensible heat fluxes or advection, and the warm rain clouds. From these results, we cannot say for sure whether the clouds lead the warming and moistening or whether the low-level warming occurs, which then leads to the clouds that enhance the warming and moistening. The second major issue is that while the results show that the anomalies in cloud LWP of precipitating clouds are coincident with moistening, it is not clear what role turbulent mixing plays in this moistening. The amount of extra cloud water available for evaporation prior to the TDs is not nearly enough to explain the observed increases in moistening. The maximum anomalies in total precipitable water are about 1 to 2 mm prior to the deep convection, however, even if all of the anomalous cloud water is evaporated it would only account for about 0.1 mm or 10 % of the total increase in moistening. It may be that while evaporation of some of the excess cloud water contributes to this moistening, turbulent mixing may make an even larger contribution. Due to the sampling limitation of the TRMM satellite it cannot be examined here, however, this idea is not necessarily inconsistent with our results. It is possible that the less efficient precipitation process

leading to enhanced cloud LWP also changes the lifetime of the clouds. Because less of the cloud water has been depleted by precipitation, it may be that the cloud is more long-lived and more moistening through mixing can occur. This will be the subject for future investigations using geostationary satellite data where the timescales of the clouds can be observed.

Finally, while there are obvious differences in anomalies of cloud LWP of precipitating clouds between low and high SST TD events, clearly SST is not the only factor that affects the properties of warm rain clouds. SST has small variations over the course of the TD events, however, large changes opposite to the mean variability found in LWP with SST also occur throughout the passage of the TDs. Prior to TDs when SST is approximately 0.1 K higher than the mean, cloud LWP of precipitating clouds increases and after the TD when SST is about 0.1 K lower than the mean, it decreases. More work is needed to unravel the different factors that influence warm rain cloud microphysical processes and how the relationship between precipitation and cloud production interacts with the dynamical environment to modify deep convection.

Chapter 5

Conclusions

One of the most important goals of this study was to answer questions regarding the effects that the precipitation process has on properties of warm clouds. A new combined, multi-sensor optimal estimation algorithm was developed using TRMM satellite observations to retrieve the cloud LWP of warm clouds when they are precipitating. A thorough understanding of the sensitivities and uncertainties in the retrieval was required. One important aspect of the input data to this retrieval algorithm had larger than expected consequences and was presented in Chapter 2. So that each of the microwave channels viewed the same scene, each microwave frequency was matched to 19-GHz channel FOV. Resampling the data to a common resolution exposed one of the most significant issues in microwave retrievals of cloud properties - the beam-filling effect. Differences in using native resolution T_{BS} and resampled T_{BS} in retrievals of cloud LWP were found to be about 30%, with this difference being highly related to differences in cloud fraction between the native 85-GHz FOV and the resampled 19-GHz FOV. Using a synthetic retrieval, the high frequency channels at 37 and 85 GHz were found to be responsible for the large differences in LWP. Differences in wind speed were also related to the resampling of the 10-GHz channel, as well as the 85-GHz channel, which altered the wind speed as compensation for retrieving lower LWP.

The results from Chapter 2 illustrate an extremely important problem in microwave cloud property retrievals. This had to be considered when developing a retrieval for clouds that may not fill the large microwave footprints, like the warm rain clouds of interest in this study. To overcome the beam-filling problem shown in Chapter 2, the algorithm described in Chapter 3 used visible and infrared data from VIRS to compute the cloud fraction within the resampled microwave FOVs. By using the VIRS data as a cloud mask, the contribution of the cloudy area T_{BS} to the total simulated T_{BS} could be weighted by the cloud fraction in the forward model. As expected, using the cloud fraction information raised the retrieved LWP and had very little effect on TPW and wind speed.

One of the most important additions to the retrieval algorithm was the inclusion of the rainwater from the PR. By using the PR estimates to compute the emission and scattering due to the rainwater, the LWP associated with only the cloud water content was retrieved. The χ^2 diagnostic of the OE retrieval showed that both the VIRS cloud fraction and PR rainwater information improved the fit of the retrieval with the measurements. By combining the retrieved cloud LWP of precipitating clouds and the PR rainwater content, the partitioning between the cloud and precipitation and its relationship to SST could be explored.

Results from the retrieval algorithm described in Chapter 3 showed that the cloud LWP of warm rain clouds decreases with increasing SST, in agreement with previous studies. The ratio of cloud LWP to PR rainwater was also shown decrease with SST in warm rain clouds. Together, these two results showed that as the surface temperature increases, cloud water is more efficiently converted to precipitation so that less cloud

water is available to moisten the lower and middle troposphere. Many studies have shown that moistening and preconditioning of atmosphere occurs prior to and may be necessary for the onset of deep convection. Since this preconditioning is clearly related to the amount of cloud water available to evaporate and moisten the low and mid levels, the retrieval algorithm described in Chapter 3 provided a new way to examine the part that precipitating clouds play in this preconditioning.

To investigate the relationship between the properties of warm precipitating clouds and the preconditioning, deep convective events associated with TDs were identified. TDs occur at short timescales of three to six days, so anomalies in the thermodynamic structure and the retrievals of LWP were composited from three days prior to three days after the precipitation maxima. At all three locations spanning the Pacific Ocean, temperature and humidity both exhibited positive anomalies in the lower and mid levels prior to the onset of deep convection. This moistening and warming was also coincident with positive anomalies in cloud LWP of precipitating clouds, but almost no difference in non-raining cloud LWP. Together, these results suggest that the moistening and warming is related to the enhanced LWP in raining clouds, rather than the non-raining clouds. As the anomalies in cloud LWP of precipitating clouds increase and the low and mid levels are moistened and warmed, a resultant increase in CAPE values occurs. This destabilization and preconditioning of the atmosphere increases until the deep convection associated with the TD depletes the moisture and cools the lower and mid levels.

The results of the retrieval algorithm in Chapter 3 showed that the cloud LWP of precipitating clouds was highly related to the SST. Separating the TD events by the mean

SST supported these findings and showed that cloud LWP anomalies were lower during higher SST TDs due to the more efficient precipitation process depleting more of the cloud water. The results from separating the high and low SST TD events further supports our conjecture that the anomalies in cloud LWP of precipitating clouds are related to the moistening and heating of the lower and mid levels and subsequent increases in instability and CAPE. When the SSTs were low, less efficient precipitation processes resulted in higher anomalies in cloud LWP of precipitating clouds, which meant that more cloud water was available for moistening as shown by the larger positive humidity anomalies at low and mid-levels. More moistening and heating for low SST TD events resulted in more instability and higher CAPE values. Combined with the findings from Chapter 3, it is clear that SST plays an important role in the relationship between precipitation and cloud water and that this affects warm rain clouds' ability to help moisten and destabilize the atmosphere for deep convection.

This study focused on understanding the role of warm rain systems in the Tropics. A clear link between SST and the partitioning between cloud water and precipitation in warm rain clouds was shown. Results from the algorithm developed in this work also highlight the importance of moistening and heating from warm, precipitating convection in the destabilization of the atmosphere prior to the onset of deep convection associated with TDs. These results are similar to that shown by Benedict and Randall (2007) for the MJO, although they operate on a much a shorter timescale of one to three days in TDs, rather than one to three weeks for the MJO. While the findings from this study show a strong link between temperature, cloud and precipitation properties, and atmospheric instability prior to deep convection, obviously there is further study to be done. Results

show that positive LWP in warm precipitating clouds are coincident with moistening, however it is not clear whether the moistening is due to more water available for evaporation or due to the fact that the higher LWP clouds may be more long-lived and more mixing can occur. Another issue to address is that despite more instability for lower SST TDs, the associated deep convection was actually weaker due to wind shear. Across the passage of the TDs, a strong change in the cloud LWP of precipitating clouds occurred despite very small variations in SST. Both of these results indicate that small-scale cloud and atmospheric processes cannot be decoupled from other large-scale dynamical processes. How other environmental variables affects warm rain clouds and how other factors that influence the timing and strength of deep convection interact with the preconditioning effects of warm, precipitating clouds remain areas for future investigations.

The work presented here also provides another example of why there is such difficulty in assessing cloud feedback effects. While many feedback studies tend to make the assumption that one particular process is dominant (Stephens 2005), i.e., the longwave effect due to deep convective anvil cirrus, other effects are considered secondary. However, this work suggests that the interdependence of different types of precipitating cloud systems cannot be ignored, since the behavior of warm, precipitating clouds obviously influences the deep convection. Although other dynamical processes and forcings cannot be neglected, clearly warm, shallow convection plays a role in the timing and strength of deep convection. With such complicated interactions, more work is necessary to ascertain the different factors that influence warm rain cloud properties and how much control cloud microphysical and precipitation processes exert on the

atmospheric hydrologic cycle and cloud radiative feedback effects. For climate models to more accurately estimate future climate sensitivity, a better representation of warm rain clouds and their feedbacks on the environment and deep convection will be necessary.

References

- Backus, G. and F. Gilbert, 1970: Uniqueness in the inversion of inaccurate gross earth data. *Phil. Trans. Roy. Soc. London*, **A266**, 123-192.
- Benedict, J.J., and D.A. Randall, 2007: Observed characteristics of the MJO relative to maximum rainfall. *J. Atmos. Sci.*, **64**, 2332–2354.
- Berg, W., T. L'Ecuyer, and C. Kummerow, 2006: Rainfall climate regimes: The relationship of regional TRMM rainfall biases to the environment. *J. Appl. Meteor.*, **45**, 434 - 454.
- Bladé, I. and D. L. Hartmann, 1993: Tropical intraseasonal oscillations in a simple nonlinear model. *J. Atmos. Sci.*, **50**, 2922-2939.
- Bremen, L. V., E. Ruprecht, and A. Macke, 2002: Errors in liquid water path retrieval arising from cloud inhomogeneities: The beam-filling effect. *Meteor. Z.*, **11**, 13–19.
- Chiu, L.S., G.R. North, D.A. Short, and A. McConnell, 1990: Rain estimation from satellites: Effect of finite field of view. *J. Geophys. Res.*, **95**, 2177-2185.
- Cho, H.R., and Y. Ogura, 1974: A relationship between cloud activity and the low-level convergence as observed in Reed-Recker's composite easterly waves. *J. Atmos. Sci.*, **31**, 2058–2065.
- Deblonde, G. and S. J. English, 2001: Evaluation of the FASTEM-2 fast microwave ocean surface emissivity model. *Tech. Proc. ITSC-XI, Budapest, Hungary, 20-26 Sept. 2000*, 67-78.

- Del Genio, A.D., W. Kovari, M.S. Yao, and J. Jonas, 2005: Cumulus microphysics and climate sensitivity. *J. Climate*, **18**, 2376–2387.
- Dunkerton, T. J., and M. P. Baldwin, 1995: Observation of 3–6 day meridional wind oscillations over the tropical Pacific, 1973–1992: Horizontal structure and propagation. *J. Atmos. Sci.*, **52**, 1585–1601.
- Durre, I., R. S. Vose, and D. B. Wuertz, 2006: Overview of the Integrated Global Radiosonde Archive. *J. Climate*, **19**, 53–68.
- Elsaesser, G. S. and C. D. Kummerow, 2008: Towards a fully parametric retrieval of the non-raining parameters over the global oceans. *J. Appl. Meteor. Clim.*, **47**, 1599–1618.
- Farrar, M. R., and E. A. Smith, 1992: Spatial resolution enhancement of terrestrial features using deconvolved SSM/I microwave brightness temperatures. *IEEE Trans. Geosci. Remote Sens.*, **30**, 349–355.
- Graves, E. G., 1993: A model for the beam-filling effect associated with the microwave retrieval of rain. *J. Atmos. Oceanic Technol.*, **10**, 5–14.
- Greenwald, T. J., S. A. Christopher, and J. Chou, 1997: Cloud liquid water path comparisons from passive microwave and solar reflectance satellite measurements: Assessment of sub-field-of-view cloud effects in microwave retrievals. *J. Geophys. Res.*, **102**, 19585–19596.
- Ha, E. and G. R. North, 1995: Model studies of the beam-filling error for rain-rate retrieval with microwave radiometers. *J. Atmos. Oceanic Technol.*, **12**, 268–281.
- Hartmann, D. L., and K. Larson, 2002: An important constraint on tropical cloud - climate feedback, *Geophys. Res. Lett.*, **29**, 1951–1954.
- Haynes, J., 2008: The near-global distribution of light rain from CloudSat. Ph.D. Dissertation, Dept. of Atmospheric Science, Colorado State University, 229 pp.

- Hu, Q. and D. A. Randall, 1994: Low-frequency oscillations in radiative-convective systems. *J. Atmos. Sci.*, **51**, 1089-1099.
- Huffman, G.J., R.F. Adler, M.M. Morrissey, D.T. Bolvin, S. Curtis, R. Joyce, B. McGavock, and J. Susskind, 2001: Global precipitation at one-degree daily resolution from multisatellite observations. *J. Hydrometeor.*, **2**, 36–50.
- Iguchi, T., T. Kozu, R. Meneghini, J. Awaka and K. Okamoto, 2000: Rain-profiling algorithm for the TRMM precipitation radar. *J. Appl. Meteor.*, **39**, 2038-2052.
- IPCC, 2007: Climate Change 2007: The Physical Science Basis. Contribution of Working Group I to the Fourth Assessment Report of the Intergovernmental Panel on Climate Change [Solomon, S., D. Qin, M. Manning, Z. Chen, M. Marquis, K.B. Averyt, M. Tignor and H.L. Miller (eds.)]. Cambridge University Press, Cambridge, United Kingdom and New York, NY, USA, 996 pp.
- Johnson, R. H., P. E. Ciesielski, and J. A. Cotturone, 2001: Multiscale variability of the atmospheric mixed layer over the western Pacific warm pool. *J. Atmos. Sci.*, **58**, 2729-2750.
- _____, T. M. Rickenbach, S. A. Rutledge, P. E. Ciesielski, and W. H. Schubert, 1999: Trimodal characteristics of tropical convection. *J. Climate*, **12**, 2397-2418.
- Kalnay, E., Kanamitsu, M., Kistler, R., Collins, W., Deaven, D., Gandin, L., Iredell, M., Saha, S., White, G., Woollen, J., Zhu, Y., Leetmaa, A., Reynolds, B., Chelliah, M., Ebisuzaki, W., Higgins, W., Janowiak, J., Mo, K.C., Ropelewski, C., Wang, J., Jenne, Roy, Joseph, Dennis. 1996: The NCEP/NCAR 40-Year Reanalysis Project. *Bull. Amer. Meteor. Soc.*, **77**, pp. 437-472.
- Kemball-Cooke, S. R. and B. C. Weare, 2001: The onset of convection in the Madden-Julian oscillation. *J. Climate*, **14**, 780-793.
- Khairoutdinov, M., and Y. Kogan, 2000: A new cloud physics parameterization in a large-eddy simulation model of marine stratocumulus. *Mon. Wea. Rev.*, **128**, 229–243.

- King, M. D., S.-C. Tsay, S. E. Platnick, M. Wang, and K.-N. Liou, 1997: Cloud retrieval algorithms for MODIS: Optical thickness, effective particle radius, and thermodynamic phase. MODIS Algorithm Theoretical Basis Document No. ATBD-MOD-05, MOD06- Cloud product, 83 pp.
- Kohn, D. J., 1995: Refinement of a semi-empirical model for the microwave emissivity of the sea surface as a function of wind speed. M.S. Thesis, Dept. of Meteorology, Texas A&M University, 44 pp.
- Kummerow, C., 1998: Beamfilling errors in passive microwave rainfall retrievals, *J. Appl. Meteorol.*, **37**, 356-370.
- _____, W. Barnes, T. Kozu, J. Shiue, and J. Simpson, 1998: The tropical rainfall measuring mission (TRMM) sensor package, *J. Atmos. and Ocean Tech.*, **15**, 808-816.
- Lau, K. M. and H.T. Wu, 2003: Warm rain processes over tropical oceans and climate implications. *Geophys. Res. Lett.*, **30**, 2290-2294.
- _____, _____, Y. C. Sud, and G. K. Walker, 2005: Effects of cloud microphysics on tropical atmospheric hydrologic processes and intraseasonal variability. *J. Climate*, **18**, 4731-4751.
- Lau, N.C., and M.W. Crane, 1995: A satellite view of the synoptic-scale organization of cloud properties in midlatitude and tropical circulation systems. *Mon. Wea. Rev.*, **123**, 1984-2006.
- Liebe, H. J., G. A. Hufford, and T. Manabe, 1991: A model for the complex permittivity of water at frequencies below 1 THz. *International J. of Infrared and Millimeter Waves*, **12**, 659-675.
- _____, _____, and M. G. Cotton, 1993: Propagation modeling of moist air and suspended water particles at frequencies below 1000 GHz. *Atmospheric Propagation Effects through Natural and Man-Made Obscurants for Visible and Mm-Wave Radiation* (AGARD-CP-542). AGARD, Neuilly sur Seine, France, 195 pp.

- Lindzen, R. S., M.-D. Chou and A. Hou, 2001: Does the earth have an adaptive infrared iris? *Bull. Amer. Meteor. Soc.*, **82**, 417-432.
- Long, D. G. and D. L. Daum, 1998: Spatial resolution enhancement of SSM/I data. *IEEE Trans. Geosci. Remote Sens.*, **36**, 407– 417.
- Marshall, J. S. and W.M. Palmer, 1948: The distribution of raindrops with size. *J. Meteor.*, **5**,165-166.
- Melitta, J. and K. B. Katsaros, 1995: Using coincident multispectral satellite data to assess the accuracy of special sensor microwave imager liquid water path estimates. *J. Geophys. Res.*, **100**, 16333-16339.
- Nakajima, T. and M. D. King, 1990: Determinations of the optical thickness and effective particle radius of clouds from reflected solar radiation measurements. Part I: Theory. *J. Atmos. Sci.*, **47**, 1878–1893.
- Nakajima, Y. T., and T. Nakajima, 1995: Wide-area determination of cloud microphysical properties from NOAA AVHRR measurements for FIRE and ASTEX Regions. *J. Atmos. Sci.*, **23**, 4043-4059.
- O'Dell, C.W., F.J. Wentz, and R. Bennartz, 2008: Cloud liquid water path from satellite-based passive microwave observations: A new climatology over the global oceans. *J. Climate*, **21**, 1721–1739.
- Petersen, W. A., R. Cifelli, D. J. Boccippio, S. A. Rutledge, and C. Fairall, 2003: Convection and easterly wave structures observed in the eastern Pacific warm pool during EPIC-2001. *J. Atmos. Sci.*, **60**, 1754–1773.
- Petty, G. W., 1999: Prevalence of precipitation from warm-topped clouds over eastern Asia and the western Pacific. *J. Climate*, **12**, 220–229.
- Platnick, S., M. D. King, S. A. Ackerman, W. P. Menzel, B. A. Baum, J. C. Riédi, and R. A. Frey, 2003: The MODIS cloud products: Algorithms and examples from Terra. *IEEE Trans. Geosci. Remote Sensing*, **41**, 459-473.

- Ramanathan, V. and W. Collins, 1991: Thermodynamic regulation of ocean warming by cirrus clouds deduced from observations of the 1987 El Niño. *Nature*, **351**, 27-32.
- Rapp, A. D., C. Kummerow, and G. Elsaesser: A combined multi-sensor optimal estimation algorithm for oceanic warm rain clouds. Submitted October 2008 to *J. Appl. Meteor. Climatol.*
- _____, C. D. Kummerow, W. Berg, and B. Griffith, 2005: An evaluation of the proposed mechanism of the adaptive infrared iris hypothesis using TRMM VIRS and PR measurements. *J. Climate*, **18**, 4185-4194
- Raymond, D. J. and D. J. Torres, 1998: Fundamental moist modes of the equatorial troposphere. *J. Atmos. Sci.*, **55**, 1771-1790.
- Riehl, H., 1954: *Tropical Meteorology*. McGraw Hill, 392 pp.
- Robinson, W., C. Kummerow and W. S. Olson, 1992: A technique for matching the resolution of microwave measurements from the SSM/I instrument, *IEEE Trans. on Geosci. and Remote Sensing*, **30**, 419-429.
- Rodgers, C. D., 1976: Retrieval of atmospheric temperature and composition from remote measurements of thermal radiation. *Rev. Geophys. Space Phys.*, **4**, 609-624.
- _____, 1990: Characterization and error analysis of profiles retrieved from remote sounding measurements. *J. Geophys. Res.*, **95**, 5587-5595.
- _____, 2000: *Inverse Methods For Atmospheric Sounding: Theory and Practice*. World Scientific Publishing Co., Singapore, 238 pp.
- Rosenfeld, D. and G. Gutman, 1994: Retrieving microphysical properties near the tops of potential rain clouds by multispectral analysis of AVHRR data. *Atmos. Res.*, **34**, 259-283.

- Rosenkranz, P. W., 1998: Water vapor microwave continuum absorption: A comparison of measurements and models. *Radio Sci.*, **33**, 919-928.
- Serra, Y.L., and R.A. Houze Jr., 2002: Observations of variability on synoptic timescales in the east Pacific ITCZ. *J. Atmos. Sci.*, **59**, 1723-1743.
- _____, G.N. Kiladis, and M.F. Cronin, 2008: Horizontal and vertical structure of easterly waves in the Pacific ITCZ. *J. Atmos. Sci.*, **65**, 1266-1284.
- Short, D. A. and G. R. North, 1990: The beam filling error in Nimbus-5 ESMR observations of GATE rainfall. *J. Geophys. Res.*, **95**, 2187-2193.
- Simpson, J., C. Kummerow, W. K. Tao and R. F. Adler, 1996: On the tropical rainfall measuring mission (TRMM). *Meteor. and Atmos. Phys.*, **60**, 19-36.
- Stogryn, A., 1978: Estimates of brightness temperatures from scanning radiometer data. *IEEE Trans. Antennas Propogat.*, **AP-26**, 720-726.
- Stephens, G. L., 2005: Cloud feedbacks in the climate system: A critical review. *J. Climate*, **18**, 237-273.
- _____, P. J. Webster, R. H. Johnson, R. Engelen, T. L'Ecuyer, 2004: Observational evidence for the mutual regulation of the tropical hydrological cycle and tropical sea surface temperature. *J. Climate*, **17**, 2213-2224.
- _____, D. G. Vane, R. J. Boain, G. G. Mace, K. Sassen, Z. Wang, A. J. Illingworth, E. J. O'Connor, W. B. Rossow, S. L. Durden, S. D. Miller, R. T. Austin, A. Benedetti, C. Mitrescu, and the CloudSat Science Team, 2002: The CloudSat Mission and the A-Train: A New Dimension of Space-Based Observations of Clouds and Precipitation, *Bull. Amer. Meteor. Soc.*, **83**, 1771-1790.
- Sun, D.Z., and R.S. Lindzen, 1993: Distribution of tropical tropospheric water vapor. *J. Atmos. Sci.*, **50**, 1643-1660.
- Takayabu, Y. N., and T. Nitta, 1993: Three-to-five-day period disturbances coupled with convection over the tropical Pacific Ocean. *J. Meteor. Soc. Japan*, **71**, 221-246.

- Wentz, F. J. and T. Meissner, 2000: AMSR Ocean Algorithm ATBD Version 2. *NASA RP*, 66 pp. [Available online at http://www.ssmi.com/papers/AMSR_Ocean_Algorithm_Version_2.pdf.]
- _____, C. Gentemann, D. Smith, and D. Chelton, 2000: Satellite measurements of sea surface temperatures through clouds. *Science*, **288**, 847-850.
- Wilheit, T. T., 1979a: The effect of wind on the microwave emission from the ocean's surface at 37 GHz. *J. Geophys. Res.*, **84**, 4921-4926.
- _____, 1979b: A model for the microwave emissivity of the ocean's surface as a function of wind speed. *IEEE Trans. Geosci. Electron.*, **17**, 244-249.
- Yuter, S. E., and R. A. Houze Jr., 2000: The 1997 Pan American Climate Studies Tropical Eastern Pacific Process Study. Part I: ITCZ region. *Bull. Amer. Meteor. Soc.*, **81**, 451-481.